

General Force Sensation for Tactile Robot

Zhuo Chen^{1*}, Ni Ou¹, Xuyang Zhang¹, Zhiyuan Wu¹,
Yongqiang Zhao¹, Yupeng Wang¹, Nathan Lepora²,
Lorenzo Jamone³, Jiankang Deng^{4*}, Shan Luo^{1*}

¹Department of Engineering, King's College London, Strand, London,
WC2R 2LS, United Kingdom.

²School of Engineering Mathematics & Technology, University of
Bristol, Bristol, BS8 1QU, United Kingdom.

³Department of Computer Science, University College London, London,
WC1E 6BT, United Kingdom.

⁴Imperial College London, London, SW7 2AZ, United Kingdom.

*Corresponding author(s). E-mail(s): zhuo.7.chen@kcl.ac.uk;

jiankangdeng@gmail.com; shan.luo@kcl.ac.uk;

Contributing authors: ni.1.ou@kcl.ac.uk; xuyang.zhang@kcl.ac.uk;

zhiyuan.wu@kcl.ac.uk; yongqiang.zhao@kcl.ac.uk;

yupeng.1.wang@kcl.ac.uk; n.lepora@bristol.ac.uk; l.jamone@ucl.ac.uk;

Abstract

Robotic tactile sensors, including vision-based and taxel-based sensors, enable agile manipulation and safe human-robot interaction through force sensation. However, variations in structural configurations, measured signals, and material properties create domain gaps that limit the transferability of learned force sensation across different tactile sensors. Here, we introduce GenForce, a general framework for achieving transferable force sensation across both homogeneous and heterogeneous tactile sensors in robotic systems. By unifying tactile signals into marker-based binary tactile images, GenForce enables the transfer of existing force labels to arbitrary target sensors using a marker-to-marker translation technique with a few paired data. This process equips uncalibrated tactile sensors with force prediction capabilities through spatiotemporal force prediction models trained on the transferred data. Extensive experimental results validate GenForce's generalizability, accuracy, and robustness across sensors with diverse marker patterns, structural designs, material properties, and sensing principles. The framework significantly reduces the need for costly and labor-intensive

labeled data collection, enabling the rapid deployment of multiple tactile sensors on robotic hands requiring force sensing capabilities.

Keywords: Vision-based Tactile Sensors, Tactile Skin, Force Sensing, Robot Manipulation, Image-to-image translation

Introduction

Embodied robots capable of perceiving and interacting with environment are transforming healthcare [1, 2], manufacturing [3, 4], and service industries. While these robots rely on multiple sensing modalities, tactile sensing plays a unique and indispensable role—enabling dexterous manipulation, adaptation to unstructured environments, and safe physical interactions with humans. Yet, despite remarkable advances in vision and proprioception, replicating the sophisticated capabilities of human sense of touch in robotic systems remains a fundamental challenge, particularly for tasks demanding precise force control and dynamic tactile feedback.

Human skin is equipped with a variety of mechanoreceptors that detect mechanical stimuli, convert them into tactile signals, and transmit these signals to the somatosensory cortex for processing and recognition [5, 6]. These mechanoreceptors are categorized into slow-adapting (SA) and rapid-adapting (RA) types. Inspired by the human sense of touch, tactile robot aim to replicate these capabilities to enhance dexterity and safe human-robot interaction [7–9] shown in Fig. 1a. To achieve this, various tactile sensing systems have been developed, mimicking the mechanoreceptors embedded in human skin. These sensors can be broadly categorized into vision-based tactile sensors (VBTS)[10–12] and taxel-based tactile sensors (TBTS)[13–15]. VBTS use cameras to capture high-resolution tactile images by measuring contact geometry and surface deformation, while TBTS, such as electronic skins, record multi-channel electrical signals through diverse sensing principle, including piezoresistive[16, 17], capacitive[18], piezoelectric[19], and magnetic transductions[20]. Despite offering valuable tactile data, these highly diverse sensor types create significant domain gaps in structure design, measured signals, and material properties shown in Fig. 1b. These discrepancies complicate the integration of tactile information and hinder the consistent and adaptable sense of touch across robotic fingers equipped with homogeneous or heterogeneous tactile sensors.

The ability to unify and integrate sensory information across multiple fingers is a critical aspect of human tactile perception and motor control[21–23]—and it is equally

essential for tactile robots equipped with tactile sensors performing in-hand object manipulation tasks [24–26]. In humans, the somatosensory cortex processes and integrates tactile input from different fingers, enabling precise manipulation tasks and adaptive control of grasp forces to ensure stability and dexterity during object manipulation [27]. These capabilities are fundamental for robotic hands, where tactile feedback must dynamically adjust forces and enable interaction with objects in unstructured environments. Force sensation thus serves a dual role in robotic tactile perception: it provides crucial static and dynamic contact information while simultaneously acting as a fundamental bridge across diverse tactile sensing modalities. This bridging capability enables a quantitative and unified representation that overcomes the inherent variability in tactile sensors. Unlike raw sensor outputs—such as voltage, current, or images—which often present ambiguous or sensor-specific information, force measurements provide physically interpretable metrics that enhance both consistency and versatility in robotic applications.

Force calibration of tactile sensors. Force calibration in tactile sensors faces several fundamental challenges that impede their widespread deployment. Traditional physical-model-based methods [28, 29] and Finite Element Method (FEM) approaches [30, 31] require sensor-specific stiffness matrices or mapping functions [29]. These methods typically assume linear deformation behavior of soft elastomers under small forces, leading to degraded performance under large deformations [32, 33]. While neural-network-based methods have demonstrated superior capability in handling nonlinear responses across wide force ranges [34–36], they face their own set of challenges. The primary limitation of deep learning approaches lies in their requirement for extensive paired force-tactile datasets [34]—a constraint that introduces significant practical barriers due to the necessity of costly force/torque sensors (such as Nano17) and time-consuming data collection procedures for each new sensor. This challenge is compounded by the inevitable degradation of soft elastomers through wear and tear, necessitating frequent replacement and recalibration that disrupts continuous operation and compromises force prediction accuracy. Furthermore, the inherent variations across sensors—encompassing differences in signal modality, structural design, resolution (from electrode density in taxel-based sensors to imaging resolution in vision-based sensors), and material properties—create substantial domain gaps that prevent direct transfer of force prediction models. Consequently, the current paradigm necessitates repeated collection of paired tactile image-force data and retraining of force prediction models for each new sensor deployment.

Cross-sensor representation learning. Recent advances in transfer learning [37] and deep representation learning [38–40] have attempted to unify tactile representation or transfer tactile sensing ability, however existing approaches face significant limitations. Traditional transfer learning techniques, including fine-tuning [41], continue to require extensive labeled force data from both source and target domains. While unified representation learning methods [42, 43] show promise, they primarily focused on the GelSight sensor family and still rely on task-specific decoders trained with labeled data. Recent efforts to directly transform tactile signals between sensors [44–46] overlook crucial force information between domains and lack generalizability. Critically, current approaches fail to address both the fundamental material differences between homogeneous sensors and heterogeneous sensors in force prediction. These limitations underscore the need for a general learning framework capable of transferring force sensation capabilities across diverse tactile sensors without requiring additional force calibration data—an advancement that would significantly impact the practical deployment of tactile sensing in robotics.

Human tactile memory as inspiration. The human ability to adapt and transfer tactile sensations [47] provides valuable inspiration for developing transferrable tactile sensation in robots. The short-term tactile memory system [48, 49] enables humans to recall and transfer tactile information across different contexts and fingers. For instance, when lifting an object with one finger, humans can estimate its weight and adjust their grip using other fingers, even after a delay. This capability is rooted in the somatosensory cortex, which stores and processes tactile information to enable precise and adaptive force control [27]. Mimicking this transferrable force sensation could allow tactile robots to achieve more robust and versatile tactile sensing systems while advancing dexterity to approach human-level capabilities.

Generative learning in tactile robotics. Generative adversarial networks (GANs)[50] have been widely applied in tactile robotics for tasks such as image synthesis [51, 52] and sim-to-real skill transfer [53, 54]. By optimizing an adversarial loss, GANs enable image-to-image translation, where a generator transforms input images into target images that are indistinguishable to a discriminator. This facilitates the adaptation of skills learned in simulated environments to real-world applications, and vice versa. Recently, conditional generative models [55, 56] have enabled user-defined image editing by incorporating image conditions or text prompts, allowing for more precise tactile image synthesis [57] and simulation [58].

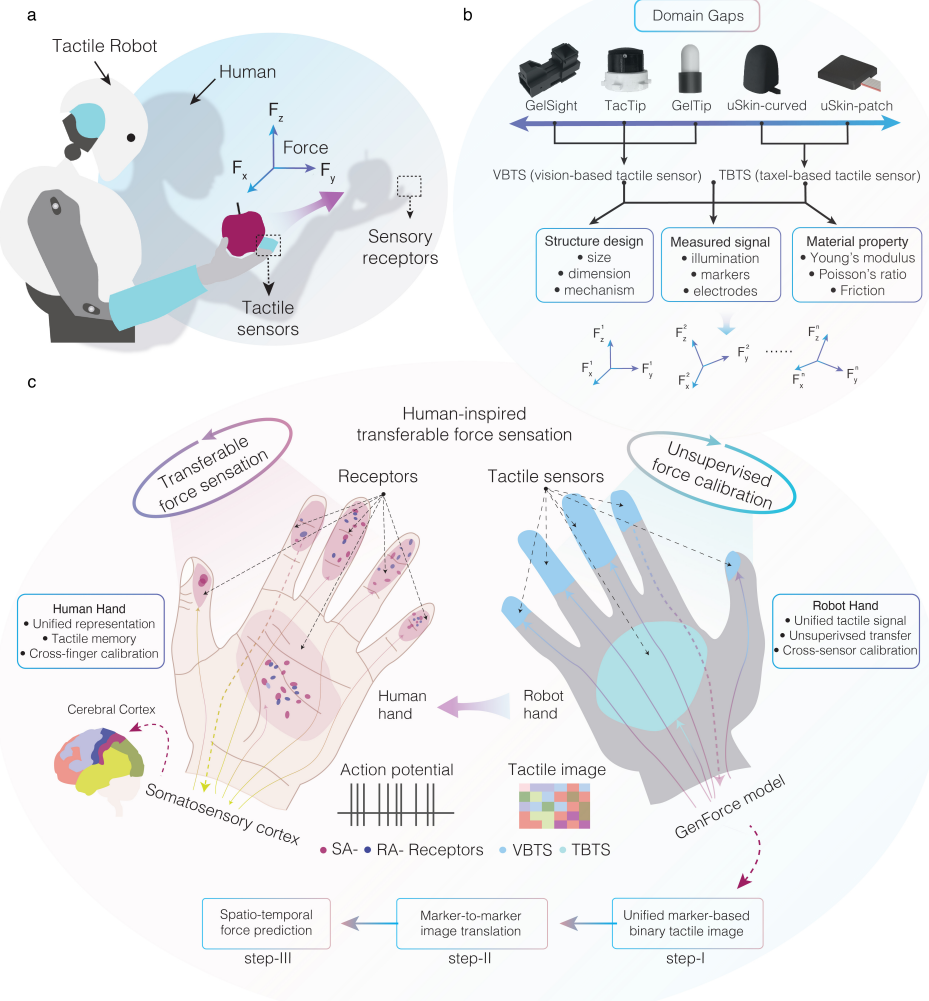


Fig. 1 Human-inspired transferable force sensation. a, The human somatosensory system seamlessly transfers force sensations across different sensory receptors in the fingers. This biological capability inspires our approach to enable tactile robots to generalize force perception from a single trained finger to multiple fingers equipped with diverse tactile sensors. b, Transferring force sensation between current tactile sensing systems—VBTS (Vision-Based Tactile Sensors) and TBTS (Taxel-Based Tactile Sensors)—remains challenging due to fundamental domain gaps in structural designs, signal modalities, and material properties. c, Our general force sensation framework, GenForce, addresses these challenges by emulating three key capabilities of the human somatosensory cortex: unified tactile representation across fingers, tactile memory formation, and cross-finger force calibration. GenForce implements unsupervised force calibration through a three-stage process: marker-based binary tactile image generation for signal unification, cross-sensor marker-to-marker translation, and spatiotemporal force prediction. This framework enables human-like force sensation transfer across homogeneous and heterogeneous tactile sensors.

Contribution

We present GenForce, a general force sensation framework that addresses a fundamental challenge in tactile robotics: achieving accurate transferable force sensation across diverse homogeneous and heterogeneous tactile sensors while overcoming domain gaps. Inspired by human transferable force sensation (Fig. 1c), GenForce mimics the human somatosensory cortex’s capabilities of unified tactile representation, tactile memory, and cross-finger calibration to achieve unsupervised force transfer and cross-sensor calibration. Our framework comprises three key components. First, we use unified marker-based binary tactile image (Fig.2a-b) to reduce measured signal gaps among sensor inputs, regardless of sensing principles, analogous to action potentials in human hands (Fig.1c). Second, marker-to-marker translation enables (Fig.2c) the transfer of existing paired force-tactile image data between different tactile sensors, eliminating the need for new force data collection—similar to human tactile memory and transfer capabilities in somatosensory cortex (Fig.1c). Third, a spatio-temporal force prediction model (Fig.4e) enhances accuracy by incorporating temporal information and material properties (Fig.6e). Extended upon our previous works [59, 60], our results show successful force translation between any sensor combinations across both homogeneous sensors (GelSight sensors with varying illumination, marker patterns, and material properties) and heterogeneous sensors (GelSight, TacTip, and uSkin), regardless of domain gaps. By significantly reducing costs while maintaining high accuracy and generalizability, our approach enables tactile robots to achieve robust force prediction capabilities, advancing the development of adaptable and cost-effective solutions for unstructured environments.

Results

Transferable force sensation

When identical three-axis forces (Fig. 2a-i) are applied to tactile sensor surfaces, both VBTS (Fig. 2a-ii) and TBTS (Fig. 2a-iii) exhibit similar skin deformation patterns (Fig. 2a-iv), varying primarily due to material properties. However, a fundamental disparity exists in their measured signals (Fig. 2b-i)—specifically between VBTS-captured images and TBTS-measured electrical signals. To eliminate these input disparities, we introduce marker-based binary tactile images (Fig. 2a-ii), which offer contact-shape insensitivity, background noise elimination, and consistent image representation. The black-and-white binary format effectively mitigates common VBTS challenges, including surface shine and illumination-induced color variations. The

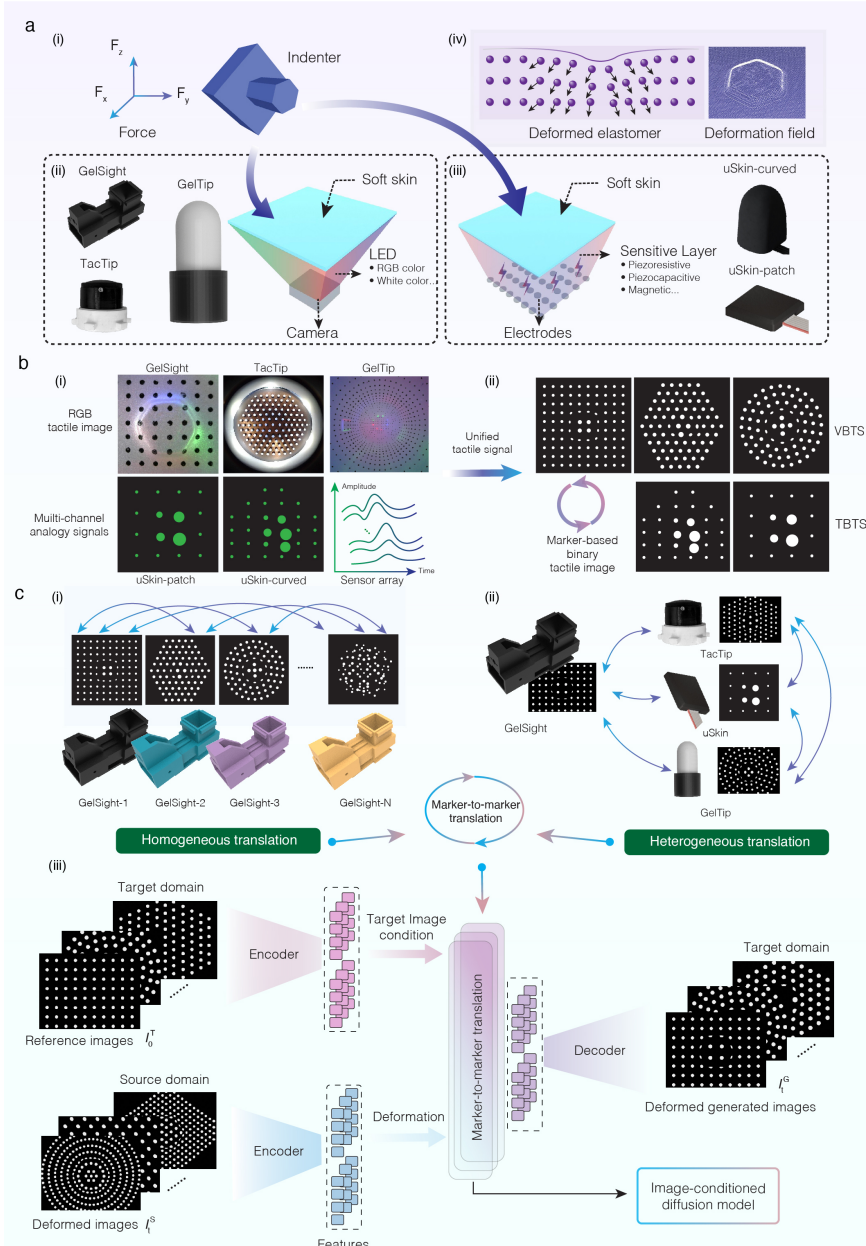


Fig. 2 Unification of tactile signals and marker-to-marker translation. a, Both VBTS and TBTS employ a sandwich-like structure analogous to human skin mechanoreceptors to perceive forces (i): a soft elastomer layer interfaces with the environment, while underlying sensing elements—cameras in VBTS (ii) and taxel electrodes arrays in TBTS (iii)—capture the resulting deformation field (iv). b, Despite their distinct sensing modalities, both systems' outputs—RGB images from VBTS (i) and multichannel analog signals from TBTS (ii)—can be transformed into marker-based binary tactile images, establishing a unified tactile representation framework. c, Cross-sensor deformation field translation is achieved through our marker-to-marker translation (M2M) model (iii), which enables bidirectional mapping between any homogeneous sensors (i) and extends to heterogeneous sensor (ii) pairs, effectively bridging the domain gap between different domain gaps.

remaining challenge lies in marker pattern differences—such as VBTS marker styles versus TBTS electrode layouts. We unify this variation through a marker-to-marker (M2M) translation technique (Fig. 2c-iii) that bridges disparities in both homogeneous (Fig. 2c-i) and heterogeneous (Fig. 2c-ii) sensors. The M2M model processes deformed images I_t^S from existing sensors (source domain S) at time steps t and reference images I_0^T from new sensors (target domain T). Using an image-conditioned diffusion model, it generates deformed images I_t^G that maintain the new sensor’s image style while preserving the existing sensor’s deformation characteristics. This enables the construction of new datasets $\{I^G, F^S\}$ from existing datasets $\{I^S, F^S\}$ to train a three-axis force ($F = \{F_x, F_y, F_z\}$) prediction model for new sensors. Similar to how humans can transfer the sense of force from any of the fingers to another in somatosensory cortex, our marker-to-marker model enables bi-directional transfer of existing force labels across multiple tactile sensors using just a single model.

Arbitrary marker-deformation generation in simulation

Training an M2M model for arbitrary marker translation requires extensive deformed marker data with diverse patterns, sizes, and densities. However, curating such marker-based binary tactile images in the real world presents significant challenges due to costly and time-intensive sensor fabrication and data collection processes. We address these limitations by pretraining M2M with simulated data (Fig. 3a) through a comprehensive simulation pipeline that generates arbitrary marker deformation images inspired by various tactile sensors including GelSight, GelTip, uSkin, and TacTip (Fig. 3b). The pipeline comprises two primary stages: material point method (MPM) simulation for generating deformed elastomer meshes, and UV mapping in Blender for marker deformation rendering. Our MPM simulation employs 18 primitive 3D indenters (Fig. 3b-i) with diverse 2D and 3D properties (vertices, edges, and curvatures), sufficient for generalizing to real-world objects, including those in the YCB dataset [61]. Using Tacchi [62], we construct a marker deformation environment where material properties (Fig. 3b-ii), indentation depths, and five distinct contact positions are precisely configured to generate deformed meshes (Fig. 3b-iii) under varying conditions. The resulting meshes are processed in Blender for marker deformation rendering. We create 12 distinct reference marker patterns (Fig. 3b-iv), named Array1-4, Circle1-4 and Diamond1-4, with varying sizes, densities, and configurations. These patterns are applied as textures to the deformed meshes’ outermost layer, with UV mapping unfolded on downward-facing normal surfaces (Fig. 3b-v). We achieve high-quality rendering through optimized lighting conditions, image resolutions, and

camera parameters—including precise location, rotation, and focal length configurations—generating marker deformation images at 480×640 resolution (Fig. 3b-vi). The resulting rendered marker images (Fig. 3b-vii) demonstrate the pipeline’s versatility and scalability across diverse deformation scenarios.

Marker-to-marker tactile image translation

The M2M model pretraining utilizes all permutations from 12 marker pattern types, yielding 132 distinct combinations. This comprehensive training approach produces a versatile pretrained model that can be efficiently fine-tuned for real-world applications. To validate the marker-to-marker translation effectiveness, we evaluate each source-to-target combination by mapping all source domain images to the target domain to generate translated images. We employ two quantitative metrics—Fréchet Inception Distance (FID) and Kernel Inception Distance (KID)—to assess image similarity between original pairs I^S, I^T and marker-to-marker translated pairs I^G, I^T . Fig. 3c-d presents heatmaps of the FID and KID results. The marker-to-marker translated image pairs demonstrate approximately 100-fold decreases in both FID and KID across all translation pairs compared to original image pairs, denoting reduced gaps in feature space. Additionally, we visualize the feature space of image pairs using t-SNE (Fig. 3e). While original image pairs from any combination show clear separation, post-translation pairs align closely in latent space, indicating that generated images become effectively indistinguishable from their target domain counterparts. Additional visualized image pairs are available in Extended Data Figure.

Homogeneous tactile force sensation

Robot hands equipped with homogeneous tactile sensors have been extensively studied in both the research community [63, 64] and commercial products [65]. In this context, we evaluate our proposed model for transferring force sensation across homogeneous tactile sensors, particularly GelSight sensors with varying configurations. We fabricate three GelSight sensors with different illumination and marker patterns (*Array-I*, *Circle-I*, *Diamond-I*) and introduce elastomer shifts to replicate long-term usage by moving or rotating *Array-I* and *Circle-I*, resulting in *Array-II* and *Circle-II*. The real-world data collection setup is shown in Fig. 4a, and the fabrication process for silicone elastomers with different marker patterns is illustrated in Fig. 4c. The detailed data collection trajectory is described in the Methods. Fig. 4b demonstrates the movement of a single contact point, covering both force increase and decrease phases in the normal and shear directions. For the experiments, we capture sequential tactile images, force

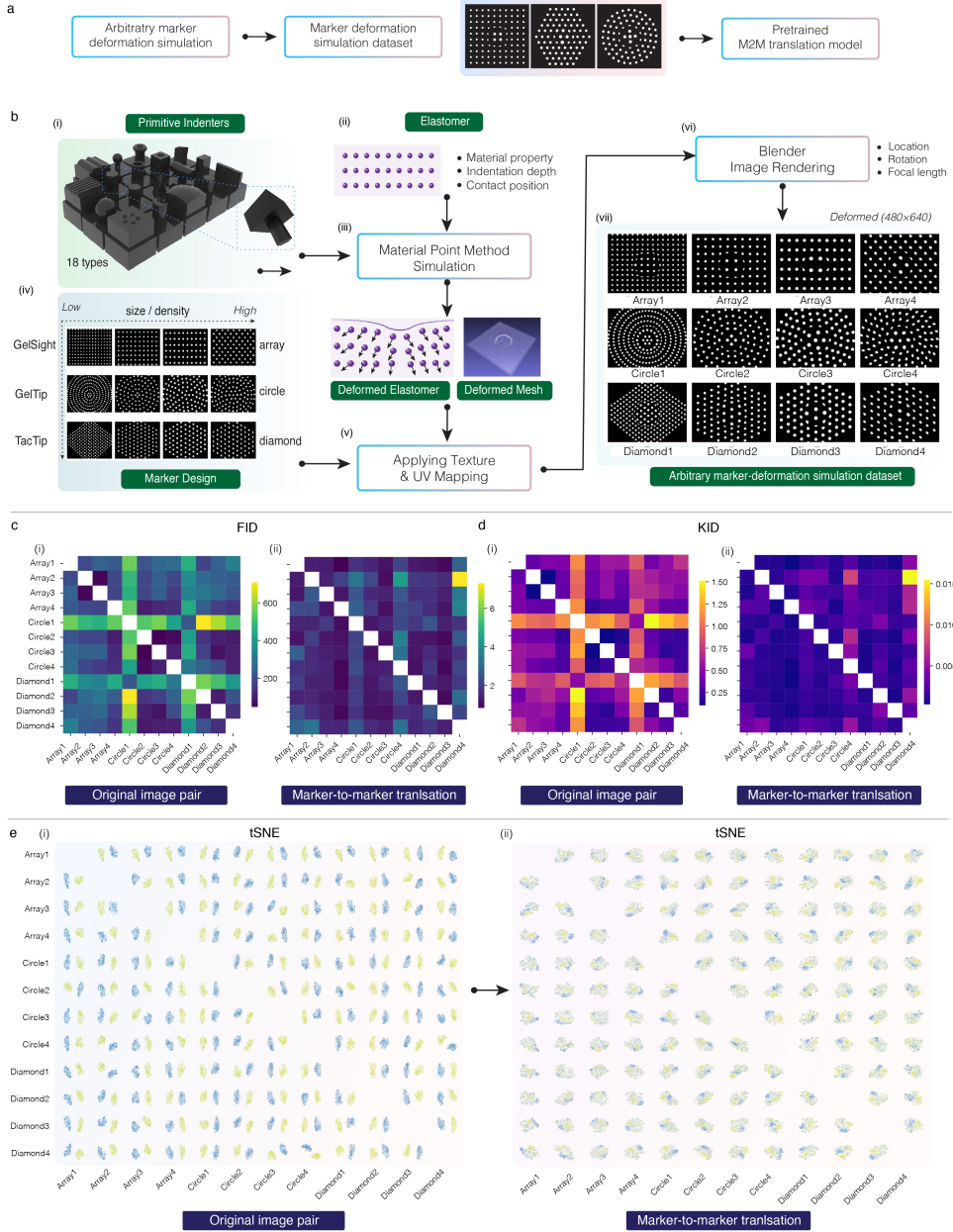


Fig. 3 Marker-to-marker translation in simulation. a, The pretrained M2M translation model is developed through three key steps: arbitrary marker deformation simulation, curation of a marker deformation simulation dataset, and pretraining of the M2M translation model. b, The pipeline (i-vii) for simulating marker deformation generates synthetic datasets with arbitrary deformed markers that are used to pre-train and evaluate the M2M model. c-d, Quantitative evaluation of the marker-to-marker translation is presented using heatmaps of FID and KID (d), comparing performance before (i) and after (ii) applying the M2M model on a simulation dataset comprising 132 different combinations. e, Feature space visualization using t-SNE illustrates improved clustering and alignment of tactile features across domains before (i) and after (ii) applying the M2M model, demonstrating its effectiveness in reducing gaps. Notably, the row labels denote S while column labels denote T in c-e.

labels, and contact poses. In addition to collecting data using a 3D support mounted on a robot arm (Fig. 4a) for *Array-II*, *Circle-II*, and *Diamond-I*, we also collect data using a simpler method by grasping the indenters with a ROBOTIQ two-finger gripper to compare the effects of installation methods on force prediction. The collected force range covers normal forces from 0 N to 18 N and shear forces from -4 N to 4 N.

To generate marker-based binary tactile images from RGB images, we utilize marker segmentation (see Methods), with the resulting marker images shown in Fig. 4d. Approximately 180,000 force-image pairs are collected per sensor for the homogeneous test, in which more than 30 tactile images are continuously collected at each contact point. For fine-tuning, we use only four contact images (the final images during the force increase and decrease phases), resulting in 17,280 location-paired images per sensor, which are ten folds less compared with force-image pairs. The location-paired images are split into 12 seen objects and 6 unseen objects. The pretrained M2M model is fine-tuned with seen objects, and all images in the force-image pairs from the source domain are transferred to the target domain for training the force prediction models in target domains. We evaluate the homogeneous translation results using image-to-image translation and force prediction, as shown in Fig. 5. For image translation, 10,000 randomly sampled images from all transferred images are used to calculate FID (Fig. 5a) and KID (Fig. 5b) across 20 combinations of 5 sensors. Similar to the simulation results, FID and KID values improve significantly, indicating alignment in the feature space. For example, when *Circle-I*, *Circle-II*, and *Diamond-I* serve as source domains and *Array-I* or *Array-II* as target domains (and vice versa), the original FID values exceed 200, and KID values are greater than 0.4. After marker-to-marker translation, these values drop by more than 98% for FID and 99% for KID. For the marker shift groups (*Array-I* to *Array-II* and *Circle-I* to *Circle-II*), similarity drops by 50%-80% in both FID and KID. The t-SNE visualization (Fig. 5c) further verifies alignment in the latent space. Detailed image-to-image translation results, divided by unseen objects, are presented in Extended Data Figure, demonstrating similar performance and the generalizability of the M2M model. Generated images for each group are provided in Extended Data Figure. Sequential tactile images aligned with deformations are shown in Supplementary Video.

Force prediction models are trained on sequential images and force pairs from seen objects after marker-to-marker translation. As we use the force labels from existing sensors, our model is unsupervised to ground truth force labels from the target domain in training stage. We evaluate force prediction performance using the coefficient of determination (R^2 , Fig. 5d) for three-axis forces $\{F_x, F_y, F_z\}$ and mean absolute errors

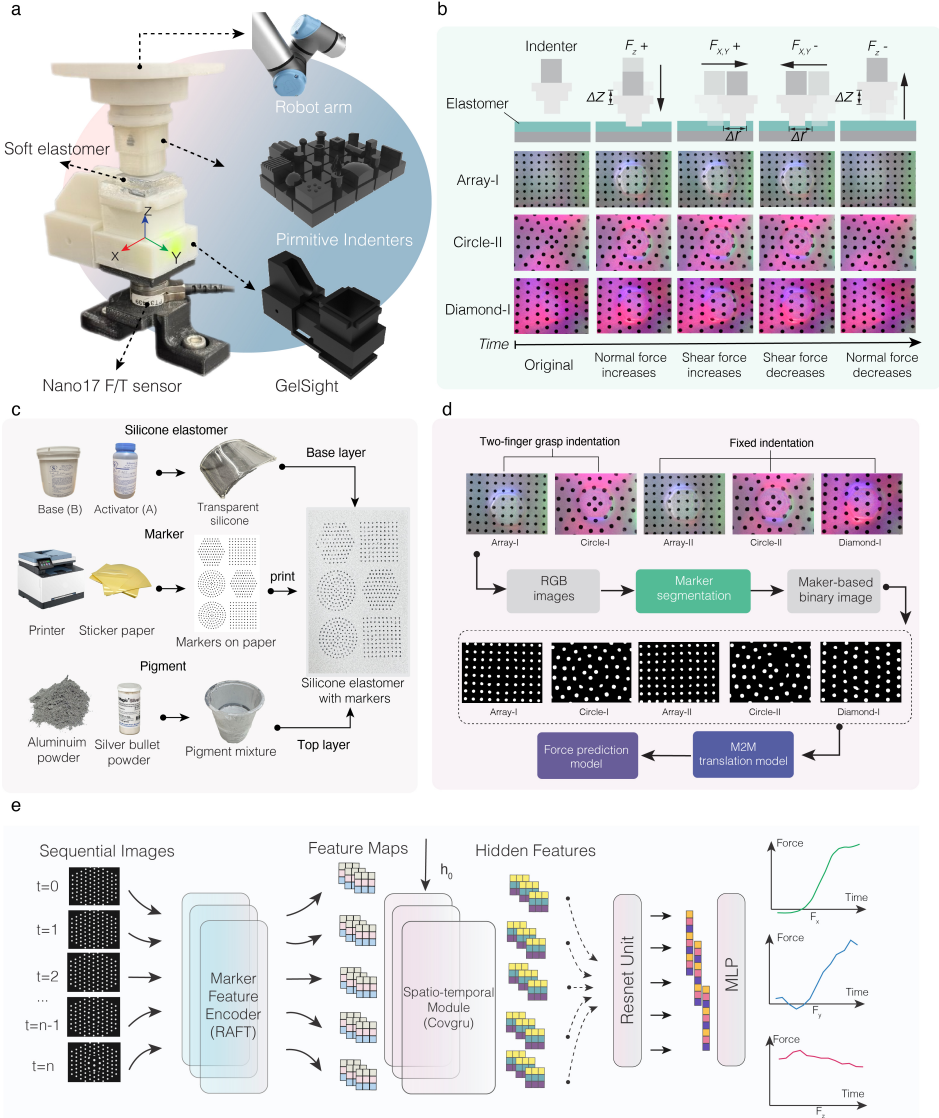


Fig. 4 Real-world data collection and force prediction model. a, The data collection setup includes a robotic arm, 18 primitive indenters, a GelSight tactile sensor, and a Nano 17 force/torque (F/T) sensor. b, Data collection trajectory for acquiring sequential tactile images under varying normal and shear forces across homogeneous GelSight sensors with different marker patterns and illumination settings. c, Fabrication process of silicone elastomers with varying marker patterns for the tested GelSight sensors. d, RGB images captured by the five GelSight sensors are preprocessed into marker-based binary tactile images to standardize tactile inputs. e, The spatiotemporal force prediction model takes sequential tactile images as input and outputs corresponding force predictions, enabling precise and robust force estimation.

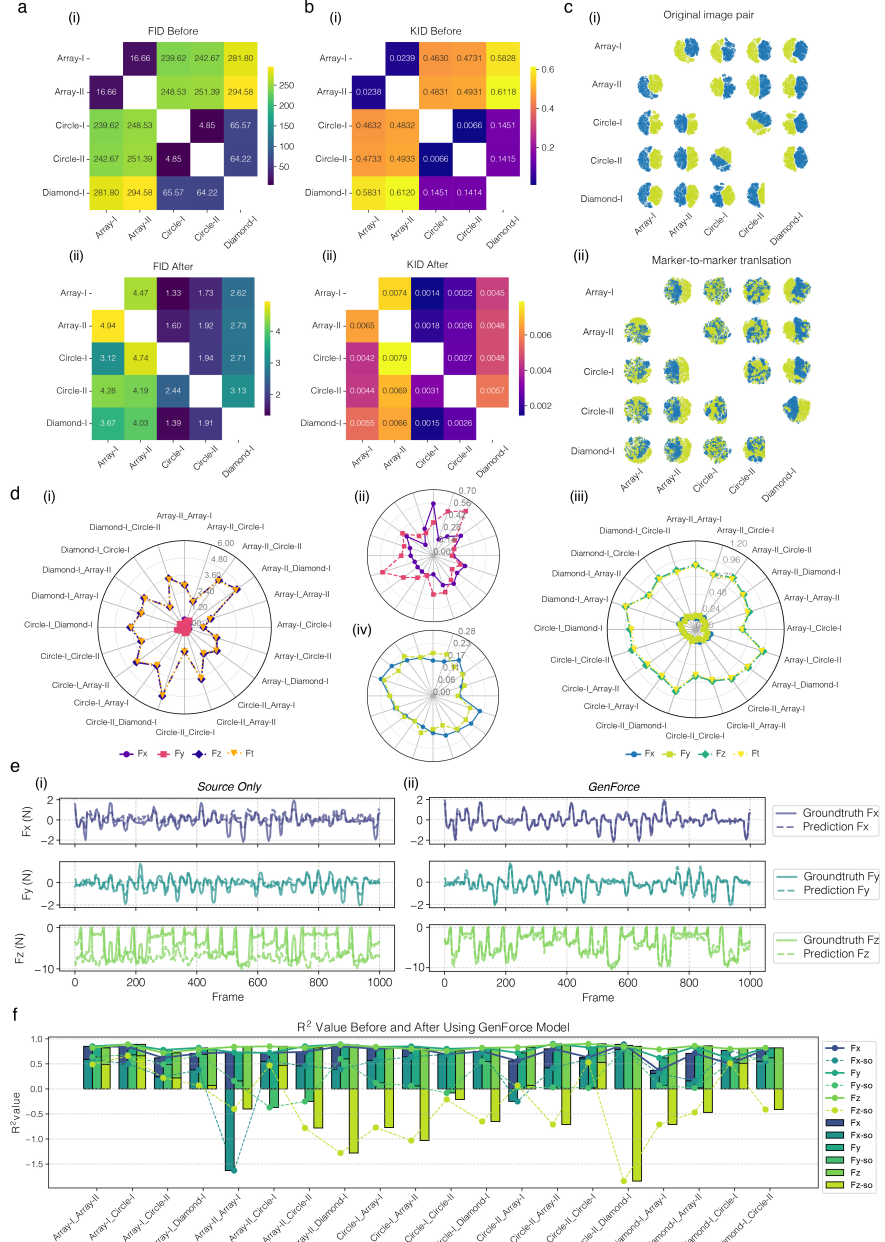


Fig. 5 Homogeneous tactile force translation results. a-b, Heatmaps of the FID (a) and KID (b) results before (i) and after (ii) using the M2M model across 20 combinations of GelSight sensors with different marker patterns. c, Feature space visualization before (i) and after (ii) applying the M2M model, showing improved alignment in feature spaces. d, Comparison of radar plots of force prediction errors before (i-ii) and after (iii-iv) using GenForce model. Note that (ii) and (iv) are zoomed-in views of F_x , F_y from (i) and (iii), respectively. F_t denotes the total force. All units are Newton (N). e, Real-time force prediction comparison over 1000 frames before (i, source only) and after using the GenForce model (ii), captured from pairs of GelSight sensor with marker *Circle-II* and marker *Diamond-I*. f, Histogram of the coefficient of determination (R^2) values for the prediction of three-axis forces, comparing the source-only (so) method and the GenForce model.

(MAE) for predicted and ground-truth forces in three-axis and total force (Fig. 5d). Without marker-to-marker translation, models trained on existing sensors and directly applied to new sensors exhibit large errors (Fig. 5d-i). For example, the maximum error in normal force exceeds 4.8 N when predicting *Diamond-I* using a model trained on *Circle-II*, with a minimum error of 1.2 N for *Array-I* to *Circle-I*. Shear force errors (F_x, F_y) for the source-only method average above 0.28 N, with a maximum error of 0.56 N for *Array-II* to *Circle-II* in F_x and *Array-II* to *Array-I* in F_y . The minimum errors remain above 0.14 N in both F_x and F_y . The R^2 histogram (Fig. 5f) shows that most source-to-target combinations have negative R^2 values, with high error variance across combinations, indicating poor performance of direct transfer models.

By contrast, after marker-to-marker translation, force prediction errors are significantly reduced, and R^2 values improve across all combinations. The radar plots (Fig. 5d-iii and Fig. 5d-iv) demonstrate reduced variance in force prediction errors across all 20 combinations. For normal force, the maximum error (observed in *Diamond-I* to *Array-I* translation) remains below 1 N, while the minimum error decreases to less than 0.7 N in *Array-I* to *Circle-II* translation. Notably, the maximum force error case (*Circle-II* to *Diamond-I*) improves from 4.8 N to 0.96 N, representing an 80% accuracy improvement. For shear forces, maximum errors in both F_x and F_y remain below 0.24 N, while minimum errors decrease to less than 0.06 N. The R^2 values (Fig. 5f) show consistent improvement across all three axes, averaging above 0.8. Random sampling of 1,000 frames from the predicted forces demonstrates well-aligned predictions with ground truth across all three axes (Fig. 5e). Additional results tested on unseen objects (Extended Data Figure) further demonstrate our model's generalizability.

Material softness effect and compensation

The deformable skin serves as the contact layer of tactile sensors, where its softness properties often change with long-term use. Additionally, material properties are customized for specific scenarios—softer skins are needed in fruit-picking while harder skins are useful for repetitive work in assembly lines. These disparities in material softness raise questions about their effects on transferrable force prediction accuracy, as the fundamental assumption in force prediction relies on using location-paired data by taking force labels from the same contact location in existing sensors as training labels for new sensors. However, this assumption introduces errors when force labels collected from tactile sensors with significantly different skin softness are applied to new sensors, as they exhibit different force-depth relationships (Fig. 6a). To address

this issue, we investigate how skin softness variation impacts force prediction accuracy using our GenForce model.

Seven groups of silicone elastomers with different material softness are fabricated as showcased in Fig. 6b by controlling the base to activator ratio (B:A). The higher the ratio, the softer the skin becomes. Additionally, we fabricate these skins with different marker patterns to approximate real sensors with varying markers. We then apply the skins on a GelSight sensor with white light, different from the homogeneous test with colored illumination, to add more variety to the test. The force-depth curve is measured during loading and unloading phases for each skin three times under 1.4 mm indentation depth with a flat rigid indenter, *prism*. The measured curves in Fig. 6c demonstrate a fundamental principle: under the same contact depth, softer skins afford smaller forces than harder skins. Furthermore, due to hysteresis properties, at the same depth, the contact force in the loading phase is greater than in the unloading phase, which leads to significant errors when predicting force using single images and encourages us to leverage temporal information. We use the same data collection method as in the homogeneous test and acquire approximately 30,000 force-paired images from each skin for force transfer and 3,400 location-paired images per skin for M2M model finetuning.

We divide the transfer direction into two groups to study material softness effects: (1) *hard-to-soft* and (2) *soft-to-hard*. Force prediction performances are evaluated using MAE and R^2 , with results shown in Fig. 6d. In the *hard-to-soft* group (Fig. 6d-i and Fig. 6d-ii), normal force prediction errors generally increase with the increase of softness gaps while R^2 decreases. For instance, when *ratio-6* (the hardest skin) serves as the source domain, force error MAE increases from a minimum of 1 N to a maximum of 2 N, while R^2 decreases from 0.8 to 0.4, indicating deteriorating performance due to increased softness gaps. For shear forces (F_x and F_y), although R^2 shows similar trends, the MAE impact is less pronounced as normal deformation dominates over shear direction, evidenced by F_z dominating total force. Conversely, the *soft-to-hard* group (Fig. 6d-iii and Fig. 6d-iv) demonstrates more stable results, with R^2 values averaging above 0.8 for both normal and shear forces regardless of softness gaps. MAE in Normal force remains below 1 N across all groups, ranging from approximately 0.6 N to 1.1 N, while shear direction MAE stays below 0.25 N. These differences compared with *hard-to-soft* group can be attributed to: (1) softness primarily affecting normal force accuracy, (2) *hard-to-soft* translation overestimating force values due to ground truth force labels exceeding target domain values, becoming more pronounced with

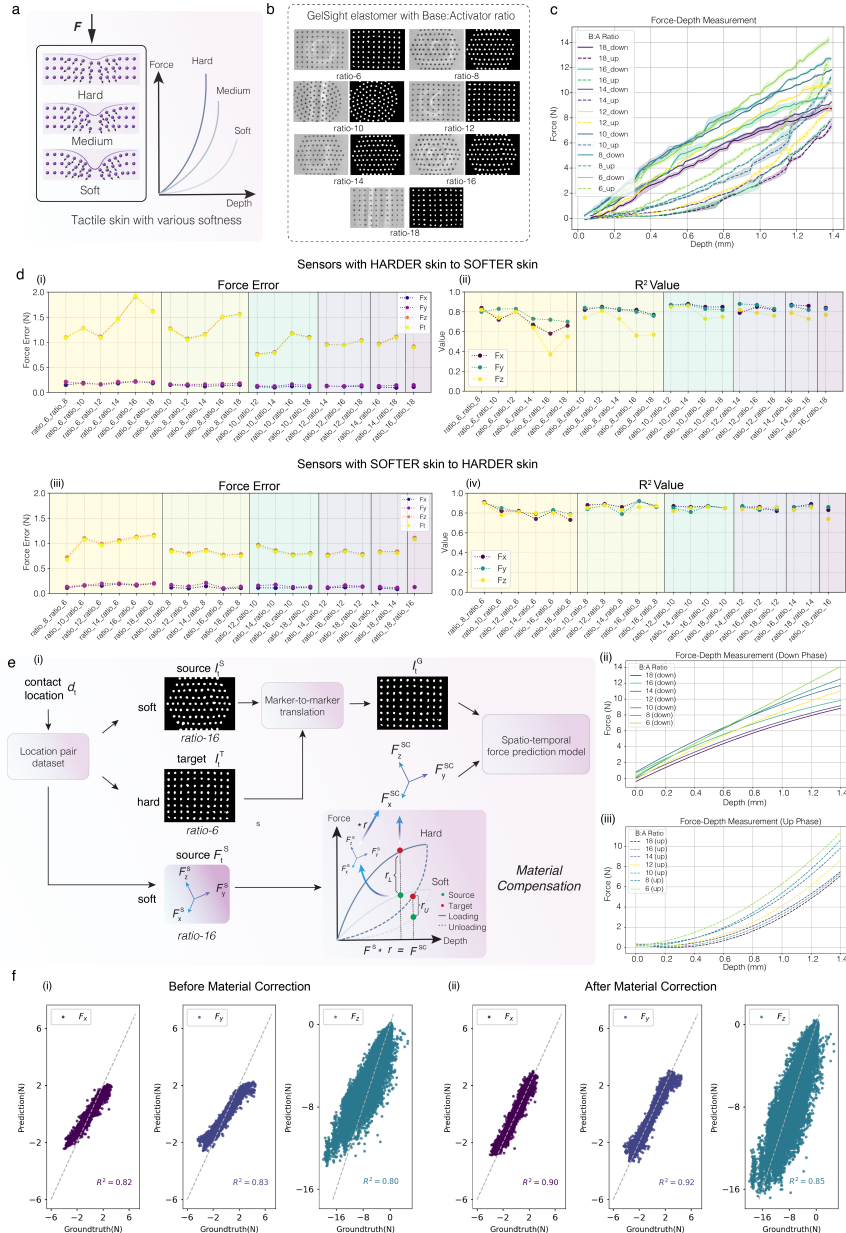


Fig. 6 Tactile skin softness effect and material compensation. a, Schematic representation of tactile skins with varying softness and their corresponding force-depth relationships. b, GelSight elastomers fabricated with seven different base-to-activator ratios, where higher ratios yield softer materials and lower ratios produce harder materials. c, Measured force-depth curves for the seven elastomers during loading (down) and unloading (up) processes, demonstrating characteristic hysteresis effects. d, Homogeneous force translation results between sensors: from harder to softer skin (i-ii) and vice versa (iii-iv). e, Material compensation process (i) incorporating material property priors to correct force labels during loading (ii) and unloading (iii) stages. f, Force prediction results demonstrating the effectiveness of material compensation when transferring from a GelSight sensor with ratio-16 (soft) skin to ratio-6 (hard) skin: before (i) and after (ii) compensation.

increasing softness gaps, and (3) *soft-to-hard* translation's underestimation having less impact than overestimation, as verified in Extended Data Figure.

To mitigate these effects, we propose a material compensation method (Fig. 6e-i) that introduces material softness priors for loading (Fig. 6e-ii) and unloading phases (Fig. 6e-iii). This approach compensates source labels F^S to F^{SC} using factors r_l (loading) or r_u (unloading) by indexing material prior with contact depth. The compensation increases force labels when transferring from softer to harder skin and decreases them in the inverse direction. Material priors are fitted with a two-degree polynomial from Fig. 6c, easily obtainable using material testing instruments or simple force gauges. Fig. 6f demonstrates force prediction results before (Fig. 6f-i) and after (Fig. 6f-ii) material compensation when transferring *ratio-16* to *ratio-6*. The under-estimation problem is successfully mitigated, improving R^2 values from 0.82 (F_x), 0.82 (F_y), 0.80 (F_z) to 0.90, 0.92, and 0.85, respectively. Extended Data Figure shows comprehensive results across other groups, with force errors reduced in 90% of harder-to-softer skin transfers and 62% of softer-to-harder skin transfers, validating our compensation method's efficacy in achieving reliable force prediction despite material softness variations.

Heterogeneous tactile force sensation

Heterogeneous tactile sensors are designed with varying sensing principles, structural configurations, and material properties, offering distinct advantages suited to specific tasks. Transferring forces across heterogeneous sensors presents additional challenges compared to homogeneous sensors due to their distinct measured signals and sensor designs (Fig. 7a). For example, the TacTip sensor, a VBTS variant characterized by embedded pin structures and liquid silicone beneath a hard 3D-printed film, allows deeper indentation depths (>5 mm) compared to GelSight sensors (<1.5 mm), which are constrained by their acrylic base and soft skin thickness. In contrast, uSkin employs magnetic transduction with a 4×4 grid of taxels, where each taxel measures 3-axis deformation and outputs multichannel analog signals with a rough skin.

To transfer force across these three heterogeneous sensor types using the GenForce model, we unify their distinct tactile signals (Fig. 2b) into binary marker-based tactile images. For TBTS, for example uSkin, we develop a signal-to-marker pipeline (Fig. 7b) that converts multichannel raw signals from each taxel into marker displacement and diameter change. Seven main hyperparameters control marker size and displacement (detailed in Extended Data Figure). For successful transfer among VBTS and other sensors, we find that the original marker size (D_{min}) should be sufficiently large due

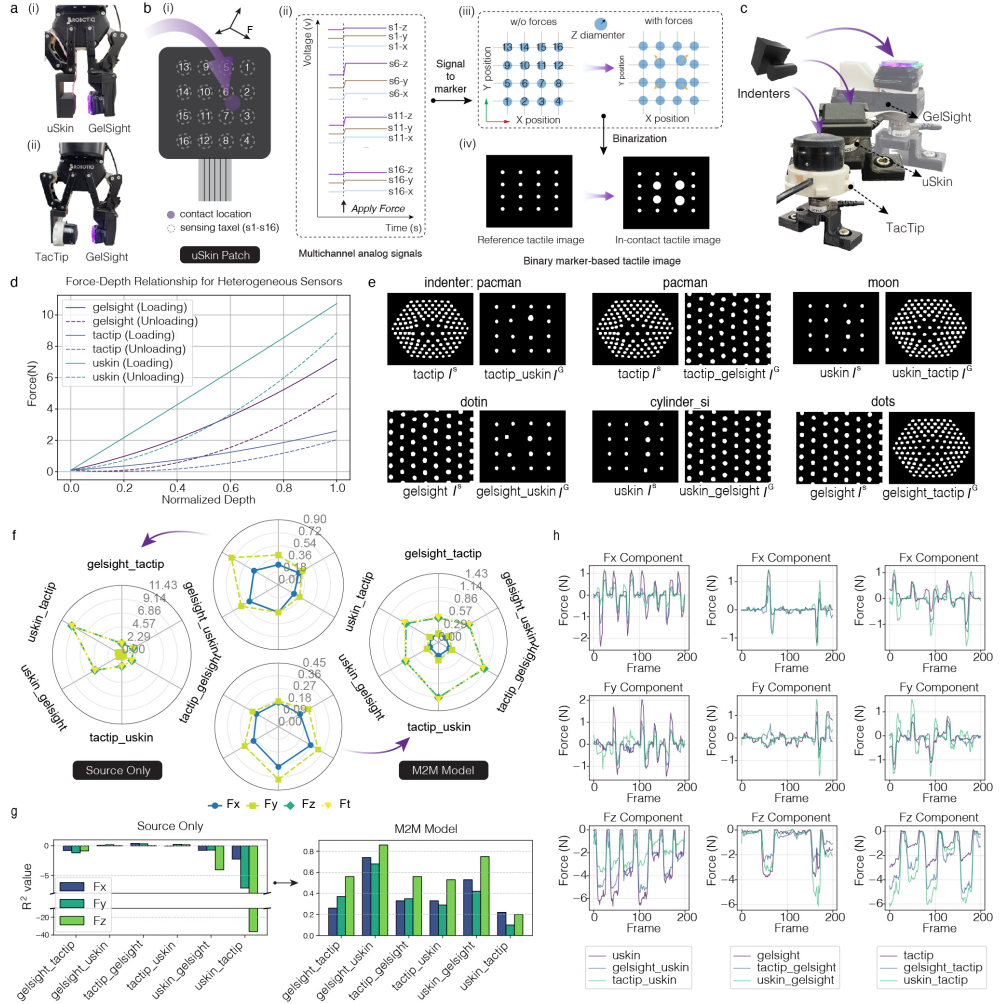


Fig. 7 Heterogeneous tactile force translation results. a, Heterogeneous configuration of a two-finger gripper with TacTip-GelSight and uSkin-GelSight tactile sensors. b, Preprocessing of TBTS data, demonstrated using a uSkin patch (i) with sixteen sensing taxels, from multichannel analog signals (ii) to marker deformation and displacement (iii), which are then converted into binary marker-based tactile images. c, Real-world data collection setup for heterogeneous force translation. d, Comparison of material softness among GelSight, TacTip and uSkin. e, Marker-to-marker translation results across three heterogeneous tactile sensors with six combinations. Source image: I^S , generated image: I^G . f, Force prediction error results before and after applying the GenForce model. g, Histogram of the coefficient of determination (R^2) values for three-axis forces before (source only) and after using the GenForce model for heterogeneous tactile sensors. h, Real-time demonstration of force prediction results in random 200 frames by setting target domain as uSkin (i), GelSight (ii), and TacTip (iii).

to uSkin’s lower resolution compared to GelSight and TacTip, while maximum size (D_{max}), lateral displacement ($\Delta X_{max}, \Delta Y_{max}$), and sensitivity parameters for size (S_D) and movement (S_X, S_Y) require careful tuning to prevent marker overlap during compression. Notably, this signal-to-marker pipeline is also applicable to other types of TBTS. For TacTip, we crop the region of interest (ROI) and extract markers using segmentation methods similar to GelSight (Extended Data Figure).

We collect heterogeneous sensor data using a setup similar to homogeneous sensors (Fig. 7c). Prior to force-image data collection, we measure force-depth relationships (Fig. 7d) for all three sensors. The skin descending softness order is established as: uSkin > GelSight > TacTip, consistent across both loading and unloading phases. We normalize contact depths for comparative analysis: 1 mm (uSkin), 1 mm (GelSight), and 4.5 mm (TacTip), accounting for TacTip’s significantly softer characteristics. Notably, despite TacTip’s deeper contact depth, its force at maximum normalized depth remains four times smaller than uSkin and two times smaller than GelSight.

For force-image paired data collection, we implement sensor-specific parameters to account for their distinct mechanical properties. For uSkin and GelSight, we set the maximum contact depth (Z_{max}) to 1 mm with a step size (ΔZ) of 0.25 mm and shear displacement (D_s) of 1 mm. For TacTip, given its softer characteristics, we use $Z_{max} = 4.5$ mm, $\Delta Z = 1.125$ mm, and $D_s = 1.5$ mm. This configuration enables image collection at 0.25 mm intervals for GelSight and uSkin to pair with TacTip collected at 1.125 mm intervals, ensuring adequate large force labels from TacTip while maintaining consistent force-normalized depth relationships across all three sensors as indexed in Fig. 7d. In total, we collect approximately 100,000 force-image paired data per sensor, with 11,520 location-paired images per sensor. We showcase several continuous frames of the raw signals of uSkin and its conversion to binary marker-based tactile images in Extended Data Figure. While the GelSight and TacTip are shown in Extended Data Figure.

The M2M translation results across three heterogeneous sensors with six combinations are showcased in Fig. 7d and Supplementary Video. Generated images (I^G) generally align well with source deformation (I^S) while exhibiting similar style to target images (I^T), validating our M2M model’s generalization to heterogeneous sensors. Several notable findings emerge regarding marker resolution. First, uSkin’s lower resolution (16 markers) compared to GelSight (56 markers) and TacTip (127 markers) creates ill-posed problems where source tactile images can generate multiple possible target images. For instance, single-taxel contact produces identical tactile images

regardless of indenter shape. Similar ill-posed conditions affect TacTip due to its hard-core outer layer's shape insensitivity, where different indentation scenarios (e.g., large sphere with shallow depth versus small sphere with greater depth) produce identical marker deformation patterns. Second, while TacTip's softness enables greater marker changes compared to uSkin and GelSight, its larger contact step combined with limited location-paired images (four in our test) introduces noise during non-location-paired image transfer.

We evaluate force prediction transfer performance using the finetuned M2M model across 100,000 force-image pairs from all three sensors. The radar plot (Fig. 7f) and histogram (Fig. 7g) demonstrate MAE and R^2 values before and after implementing our GenForce model. Direct model transfer between heterogeneous sensors shows significant errors, with maximum MAE reaching 10 N for F_z and 0.72 N for F_y , 0.2 N for F_x in the *uSkin-to-TacTip* group, while R^2 values average negative across all axes. Similar results appear in the *uSkin-to-GelSight* group, attributed to uSkin's lower resolution. The remaining four combinations average 2.29 N error for F_z and 0.36 N for F_x and F_y , with minimum errors in softer-to-harder skin transfers (*TacTip-to-GelSight* and *TacTip-to-uSkin*), consistent with our previous findings on underestimation effects.

After implementing the M2M model, force prediction accuracy improves substantially. F_z MAE decreases below 1 N across all combinations, ranging from 1.14 N (*TacTip-to-uSkin*) to 0.57 N (*GelSight-to-TacTip*), while F_y and F_x reduce below 0.36 N and 0.27 N respectively. Notably, the *uSkin-to-TacTip* group shows 91.4% improvement in F_z MAE (reduces to 0.86 N) and 75% improvement in F_y (reduces to 0.18 N). R^2 values improve across all combinations, following an ascending performance order: *GelSight-to-uSkin*, *uSkin-to-GelSight*, *TacTip-to-GelSight*, *GelSight-to-TacTip*, *TacTip-to-uSkin*, and *uSkin-to-TacTip*. This order correlates with material softness gaps and marker resolution differences. GelSight and uSkin, having similar skin softness, show lower errors compared to TacTip combinations. Additionally, uSkin's lower resolution leads to better performance when serving as a target domain rather than a source domain. Random sampling of 200 test frames (Fig. 7h) demonstrates continuous force prediction patterns consistent with material property relationships in Fig. 7d.

Discussion

GenForce introduces a general framework for transferring force sensation between calibrated and uncalibrated tactile sensors, mimicking the human ability to adapt

force perception across different fingers. This advancement addresses critical challenges in tactile robotics, offering a scalable solution for force calibration and broader implications for robotic perception.

Traditional force calibration relies on expensive and fragile Nano 17 F/T sensors, requiring extensive paired force-tactile data collection for each sensor. This process is time-intensive, memory-demanding, and impractical for repeat across diverse tactile sensors. GenForce eliminates the need for F/T sensors when calibrating new tactile sensors by leveraging existing force labels. Through marker-to-marker translation, the model requires only a fraction of location-paired tactile images, significantly reducing the time and cost of data collection while simplifying the calibration process. This efficiency enables the use of existing force labels across any combination of tactile sensors, regardless of differences in sensing principles, structural designs, or material properties, using a single M2M model for arbitrary translation.

Unlike existing approaches that rely on invariant feature-space representations—often producing unexplainable encoders, requiring extensive labeled data, and being limited to single sensor families—GenForce operates directly at the input level. By translating deformed images into well-aligned target images, the model enables direct transfer of image-force pairs while providing visual verification of deformation in the target domain. This approach bypasses constraints of sensing principles, incorporates material property compensation, and generalizes across both TBTS and VBTS sensors, effectively bridging domain gaps caused by differences in resolution, structural design, and material softness.

Experimental validation demonstrates GenForce’s generalizability across both homogeneous and heterogeneous tactile sensors. For homogeneous VBTS sensors, the model performs robustly under variations in illumination, marker patterns, and material softness. More importantly, it bridges the gap between heterogeneous sensors (VBTS and TBTS) with fundamentally different sensing principles and structural designs. Quantitative analyses of marker-to-marker translation and force prediction confirm significant error reductions across all sensor combinations, even in challenging scenarios with large material softness gaps or low-resolution sensors, accelerating the deployment of diverse tactile sensing systems.

Beyond force sensation, GenForce’s contributions—unified binary tactile signals, conditioned marker-to-marker translation, and spatio-temporal force prediction—extend to broader robotic applications. These include in-hand pose estimation, slip detection, and other tactile sensing tasks critical for dexterous manipulation. By

establishing a unified framework for transferring tactile sensations across different sensors, this work lays the foundation for human-like transferable tactile perception in robotics. The ability to seamlessly integrate heterogeneous tactile sensors into robotic systems represents a significant step toward more adaptable and versatile robots capable of interacting with complex environments.

Methods

General force sensation model

To transfer force sensation in a manner analogous to human fingers, we aim to transfer the deformation between tactile sensors by transferring the image style of marker patterns. Specifically, we assume that one tactile sensor, referred to as the source domain S , is equipped with paired force-tactile image data $\{I^S, F^S\}$, while new tactile sensors in the target domain \mathcal{T} have only tactile image data $\{I^T\}$ available. To align the image distribution between the source domain $p(I^S)$ and target domains $p(I^T)$, we train a image conditioned generator $G(I^S, I_0^T)$ to map I^S to I^T , such that $G : I^S \rightarrow I^T$. The conditional input used here is the reference image I_0^T , representing the target sensor in a non-contact state. Once the generator G is trained, I^S can be translated into I^G , which matches the image style of I^T while preserving the deformation information of I^S . This enables the creation of a new training dataset $\{I^G, F^S\}$ for training force prediction models \hat{h} . These models can then predict estimated forces F^T in the target domain while minimizing the force prediction error:

$$\arg \min_{\hat{h}} \mathbb{E}_{(I^T, F^T)} \left\| \hat{h}(I^T) - F^T \right\|_1$$

Marker-to-marker Translation. The marker-to-marker translation model addresses the challenge of translating marker-based binary tactile images from existing sensors with force labels (source domain $S \subset \mathbb{R}^{H \times W \times 3}$) to new sensors without force labels (target domain $\mathcal{T} \subset \mathbb{R}^{H \times W \times 3}$). Given image datasets $S = \{I^S \in S\}$ and $T = \{I^T \in \mathcal{T}\}$ with paired contact locations, our model learns a mapping function $G(I^S, I_0^T) : S \rightarrow T$ that transforms contact images I^S to I^T . The conditional input I_0^T serves as a reference image without contact from the new sensor, providing image-style guidance when transferring between multiple source sensors $\{S_i\}_{i=1}^N$ and target sensors $\{T_i\}_{i=1}^N$. This approach enables a single mapping function G to handle arbitrary source-target sensor pairs, eliminating the need for multiple pair-specific models.

The translation model architecture comprises two primary components: a variational autoencoder (VAE) and a latent diffusion model (LDM). The VAE transforms

contact images I_t^S at time steps $t = \{1, 2, \dots, T\}$ and the conditional image I_0^T into latent vectors z_t^S and z_t^0 for the diffusion process, subsequently converting the output latent vector z_t^G back to I_t^G with the target image style. The LDM, implemented with a U-Net architecture, fuses current contact images z_t^S with the conditional input z_t^0 through cross-attention mechanisms and denoises the fused feature map to produce latent vectors z_t^G in the target domain. This end-to-end architecture enables direct translation of marker-based binary images from I_t^S to I_t^T .

The training objective combines two primary components: an adversarial loss \mathcal{L}_{gan} and a reconstruction loss \mathcal{L}_{rec} incorporating L2 and LPIPS metrics.

Adversarial Loss. The adversarial loss aims to align the distribution of generated tactile images $p(I^G)$ with the target domain distribution $p(I^T)$. The discriminator D_T learns to differentiate between generated images I^G and real target images I^T . The adversarial loss is formulated as:

$$\mathcal{L}_{gan} = \mathbb{E}_{I^T \sim p(I^T)} [\log D_T(I^T)] + \mathbb{E}_{I^S \sim p(I^S)} [\log(1 - D_T(G(I^S, I_0^T)))] \quad (1)$$

where G minimizes this objective while D_T maximizes it: $\min_G \max_{D_T} \mathcal{L}_{gan}$.

Reconstruction Loss. The reconstruction loss \mathcal{L}_{rec} ensures both pixel-level and perceptual-level similarity between generated images I^G and target images I^T through L2 and LPIPS metrics, capturing subtle marker displacement during translation:

$$\mathcal{L}_{rec} = \mathbb{E}_{I^S \sim p(I^S)} \|I^T, G(I^S, I_0^T)\|_2 + \mathbb{E}_{I^S \sim p(I^S)} \|I^T, G(I^S, I_0^T)\|_{PIPS} \quad (2)$$

Overall Objective. The complete learning objective for the generative model combines the above losses with weights λ_{gan} and λ_{rec} :

$$\arg \min \lambda_{gan} \mathcal{L}_{gan} + \lambda_{rec} \mathcal{L}_{rec} \quad (3)$$

Spatio-temporal Force Prediction. Following marker-to-marker translation, we leverage the trained mapping function G to transform source images I^S from the existing paired force-label dataset $\{I^S, F^S\}$ into a new dataset $\{I^G, F^S\}$. This translated dataset facilitates the training of a force prediction model \hat{h} that generalizes directly to new sensors equipped with only tactile images $\{I^T\}$. Our model specifically addresses the prediction of three-axis forces $F = \{F_x, F_y, F_z\}$.

To tackle the hysteresis characteristic of silicone elastomers—where identical deformation depths yield different forces during loading and unloading phases—we develop a spatio-temporal architecture with four specialized components: (1) a RAFT-based feature encoder that extracts rich spatial representations from sequential input images ($S \times B \times C \times H \times W$) into a 128-dimensional feature space, (2) a Convolutional GRU

(ConvGRU) module that captures temporal dependencies while preserving spatial information in the feature sequence, (3) a ResNet module that hierarchically processes features through residual blocks (128→256→512 channels), progressively reducing spatial dimensions while enhancing feature abstraction, and (4) a regression head that transforms the processed features into force predictions via a sigmoid activation function.

The network is optimized end-to-end using a mean absolute error (MAE) loss function:

$$\mathcal{L}_{\text{MAE}} = \frac{1}{N} \sum_{i=1}^N \|\hat{F}_i - F_i\|_1 \quad (4)$$

where \hat{F}_i and F_i denote the predicted and ground-truth forces respectively, and N represents the batch size.

This architectural design enables comprehensive capture of both spatial deformation patterns and their temporal evolution, effectively differentiating between loading and unloading states through the ConvGRU’s memory mechanism. The hierarchical feature abstraction through the post-processing layers systematically distills force-relevant information from the spatio-temporal features, resulting in enhanced prediction accuracy across both normal and shear directions.

Simulation of marker deformation

The simulation of arbitrary marker deformation consists of two key steps: the simulation of deformed elastomer and the marker image rendering.

Simulation of deformed elastomer. We first simulated elastomer deformation using the material point method implemented in Tacchi [62]. The simulation model comprised a 20 mm × 20 mm elastomer with a thickness of 4 mm. The material properties were set to reflect typical tactile sensor characteristics, with an elastic modulus of 1.45×10^5 Pa and a Poisson’s ratio of 0.45. To generate comprehensive deformation data, we employed 18 different primitive indenters following the contact trajectory. The trajectory pattern covered a grid of contact locations with horizontal steps (ΔX , ΔY) of 4 mm and vertical increments (ΔZ) of 0.3 mm, reaching a maximum indentation depth (Z_{\max}) of 1.5 mm. This systematic approach yielded 45 contact locations (5 step in depth × 9 grid) per indenter, resulting in 810 unique deformed mesh configurations across all indenters. For each contact simulation, the indenter was initialized at a position where its bottom surface was parallel to and just above the elastomer surface. To ensure smooth contact dynamics and accurate shear deformation, we set

the world step time to 1×10^{-4} s and the contact speed to -10 mm/s, resulting in precise 0.001 mm movements per simulation step.

Marker image rendering. Upon obtaining the deformed meshes, the meshes are imported into Blender for marker image rendering. Before rendering, we draw 12 types of reference marker images with different marker patterns, density, and size using CAD software. The rendering process is automated through a custom Blender Python script that processes each deformed mesh systematically. For each mesh, we first apply UV unwrapping specifically to surfaces with negative Z-axis normals, ensuring proper texture mapping of the marker patterns. The UV coordinates are automatically adjusted through rotational alignment to maintain consistent marker orientation across all renders. The rendering environment is carefully configured with a 35 mm focal length camera, oriented downward to capture the deformed surface. To ensure optimal visibility of the marker patterns, we set the world light strength to 60.0 units and eliminate material specularity. The final renders are output as 640×480 JPEG images, with each of the 18 primitive indenters generating 45 unique deformation states, resulting in a comprehensive dataset of 810 marker images per marker pattern, totaling 9,720 images across all marker variations.

Fabrication of tactile sensors

We primarily utilized two prominent types of VBTSSs: the GelSight2014 [66] from the GelSight family and TacPalm [67] from the TacTip family, both fabricated in-house. Additionally, we incorporated an off-the-shelf TBTS, the uSkin-patched, purchased from XELA robotics. Related fabrication details for TacPalm can be found in [67].

Fabrication of GelSight. The GelSight2014 sensor integrates a Logitech C270 HD webcam, 3D-printed components (fabricated using Bambu Lab P1S), laser-cut acrylic boards, LED lights, and soft elastomers. To achieve varying illumination conditions in the homogeneous group, we attached different resistors to the LED lights, producing three distinct GelSight variants: sensors with marker *Array-II*, *Circle-II*, and *Diamond-I* patterns. The sensors *Array-I* and *Circle-I* are identical to *Array-II* and *Circle-II* respectively, differing only in their marker patterns. For material compensation testing, we utilized natural lighting instead of LEDs to evaluate our model's generalizability.

Fabrication of soft skins with various softness. The fabrication of silicone elastomers with different markers followed a three-step process. First, we mixed XPA-565 base (B) with activator (A) and poured the mixture into a 4 mm thick mold for 24-hour natural curing to obtain transparent silicone elastomer. For heterogeneous and

homogeneous tests, we used a 15:1 ratio for GelSight sensors, while material compensation tests employed seven different ratios ranging from 6:1 to 18:1, where higher ratios produced softer elastomers. Second, we printed designed markers on sticker paper using an office inkjet printer and transferred them onto the transparent elastomer. Finally, we prepared a coating mixture by combining aluminum powder and silver bullet powder (pigments) with solvent in a 1:1:2.5 ratio, then mixed this with silicone elastomer (15:1 ratio) before applying it to the masked transparent elastomer. The pigment mixture was then poured onto the elastomer to ensure opaqueness while maintaining negligible thickness. After 24 hours of curing, we extracted and cut the elastomer to 20 mm \times 20 mm dimensions for testing. Notably, increasing the XPA-565 ratio extended the required curing time.

Data Collection in Real World

The data collection setup consists of five main components: a UR5e robot arm, a Nano17 force/torque sensor, 3D-printed indenters, tactile sensors, and a support base. The indenters comprise 6 indenters in the unseen group and 12 in the seen group. Each indenter was mounted on the robot arm with fixed initial position and orientation.

Data collection trajectory. We designated five contact points across the surface, chosen to ensure comprehensive coverage of the soft elastomer. For each point, the indenters move towards different target points near this original point in normal and shear direction to execute a four-phase movement sequence: normal force increase (moving down), shear force application (moving laterally), shear force release (returning laterally), and normal force decrease (moving up). This protocol captured both increasing force processes (F_N^+, F_s^+) and decreasing force processes (F_N^-, F_s^-), where N and S denote normal and shear forces, respectively. The movement speed was set to 25% for GelSight and uSkin sensors, and 40% for TacTip on the touch panel. Images and forces were synchronized and collected in real-time at 40 Hz across all tests. The robot arm motion is shown in Algorithm 1.

Parameter setting. For homogeneous and material compensation tests, we implemented the following parameters: horizontal moving distances $\Delta x = 3$ mm and $\Delta y = 4$ mm, depth step $\Delta Z = 0.3$ mm with maximum depth $Z = 1.2$ mm, moving angle $\theta = 30^\circ$, and shear distance of 1 mm. This configuration yielded $5 \times 4 \times 12 = 240$ target points with varying moving directions and locations. For material compensation testing, data collection was limited to point 1 to expedite the process. The heterogeneous test employed a modified moving angle $\theta = 45^\circ$, with adjusted depth parameters

Algorithm 1 Real World Data Collection

```
1: Input: Number of surface contact points  $k$ , surface contact points  $P = \{P_1, \dots, P_k\}$ , where  $P_i = \{p_1, \dots, p_n\}$  contains all contact points in depth,  $p_i = \{x, y, z\}$  denotes the coordinate of a contact point.
2: procedure MOVE TO CONTACT POINTS( $P, k$ )
3:   for  $i = 0 \dots k$  do
4:      $p_0 \leftarrow P_i[0]$                                  $\triangleright$  origin point  $p_0$  without contact
5:      $moveTo(p_0)$ 
6:     for  $j = 1 \dots n$  do
7:        $p_1 \leftarrow (p_0[0], p_0[1], P_{ij}[2]), p_2 \leftarrow P_{ij}$ 
8:        $moveTo(p_1), image\_force\_pose\_record()$            $\triangleright$  Normal increases
9:        $moveTo(p_2), image\_force\_pose\_record()$            $\triangleright$  Shear increases
10:       $moveTo(p_1), image\_force\_pose\_record()$            $\triangleright$  Shear decreases
11:       $moveTo(p_0), image\_force\_pose\_record()$            $\triangleright$  Normal decreases
12:     end for
13:   end for
14: end procedure
```

for GelSight and uSkin ($\Delta Z = 0.25$ mm, maximum $Z = 1$ mm) to better align maximum depths. TacTip parameters were uniquely configured with $\Delta x = \Delta y = 6.5$ mm, $\Delta Z = 1.125$ mm, maximum $Z = 4.5$ mm, $\theta = 30^\circ$, and shear distance of 1.5 mm. This configuration yielded $5 \times 4 \times 8 = 160$ target points. The number of collected frames per contact point ranged from 20 to 60, depending on moving distance. The total dataset comprised approximately 180,000 images per sensor in heterogeneous tests, 35,000 images per sensor in material tests, and 11,000 images per sensor in homogeneous tests.

Marker Segmentation. The marker segmentation process consists of two main stages: rough extraction and fine extraction. In the rough extraction stage, we first define a region of interest (ROI) mask to isolate the relevant marker area. The raw RGB images undergo brightness normalization using histogram equalization in the YUV color space. Black markers are then identified using intensity thresholding followed by morphological operations. In the fine extraction stage, we employ an EfficientSAM [68] model to precisely segment individual markers. The model processes marker candidates within bounding boxes centered on the roughly detected marker positions. The resulting binary masks are processed to obtain the final marker positions, which are stored as binary-valued array for subsequent marker-to-marker translation tasks and force prediction tasks. This two-stage approach ensures robust marker detection across varying lighting conditions and sensor configurations.

Marker conversion for uSkin. The uSkin patch sensor consists of a 4×4 grid of taxels, where each taxel measures 3-axis deformation (normal and shear). The sensor data is streamed through a WebSocket connection at 60Hz, with each frame containing 16 three-dimensional vectors representing the taxel deformations. We visualize the sensor data in real-time using a scatter plot where the position of each marker represents the shear deformation (x,y) and the marker size indicates the normal force (z). Through extensive experimentation, we determined the optimal visualization parameters for each axis: for shear deformations (x,y), we apply scaling factors $S_x = S_y = 2 \times 10^{-4}$ with displacement limits of ± 0.6 units from the base grid positions, constraining the total visualization range to $[-0.6, 3.6]$ units to maintain grid structure. For normal forces (z), we employ a scaling factor $S_z = 0.2$ with marker sizes bounded between 300 and 6000 pixels, ensuring clear visibility of both light and firm contacts. These carefully tuned parameters provide an optimal balance between sensitivity to subtle deformations and clear visualization of larger forces while preventing marker overlap or grid distortion. The raw sensor values are normalized by subtracting a reference frame captured at the start of data collection to account for initial offsets. During each phase, we simultaneously record: (1) uSkin tactile images (640×480 pixels) and raw 3D deformation values, (2) 6-axis force/torque measurements from an ATI Nano17 sensor, and (3) 6D robot end-effector poses. The data is collected at a controlled frequency of 60Hz.

Marker-to-marker Translation Model

The marker-to-marker translation model consists of two main components: a marker encoder-decoder and an image-conditioned diffusion model.

Marker encoder-decoder. For the marker encoder-decoder, we adopt the variational autoencoder (VAE) architecture from SD-Turbo [69, 70], enhanced with Low-Rank Adaptation (LoRA) for efficient fine-tuning. The VAE processes marker images of size 256×256 pixels and employs a dual-path structure: an encoder that compresses marker patterns into a latent space, and a decoder that reconstructs marker patterns from these latent representations. To optimize the model’s performance while maintaining parameter efficiency, we implement LoRA with rank-4 adaptation on key network components, including convolutional layers and attention mechanisms. The training objective combines reconstruction loss (L1 and L2) with a KL divergence term to balance accurate pattern reconstruction with latent space regularization. This architecture enables effective compression of marker patterns into a structured latent

space while preserving essential geometric and spatial relationships between different marker types.

Image-conditioned diffusion model. The second component of our translation model is an image-conditioned diffusion model based on SD-Turbo architecture, which consists of a UNet backbone and a specialized noise scheduler. We implement a single-step diffusion process using a modified DDPMsScheduler, optimized for efficient marker pattern translation. The UNet model is augmented with LoRA adaptation (rank-8) applied to key network components, including attention layers, convolutional layers, and projection layers. The translation process operates in the latent space, where marker patterns I_t^S from source domains S and reference patterns I_0^T from target domains T are first encoded through their respective VAEs. Notably, the source pattern I_t^S is encoded through the trainable marker encoder to produce latent \mathbf{z}_t^S , while the target pattern is processed by a frozen reference encoder to generate conditioning latent \mathbf{z}_0^T . The UNet then performs guided denoising, taking \mathbf{z}_t^S as input and \mathbf{z}_0^T as cross-attention condition for efficient processing. The denoised latent is finally decoded through the trainable marker decoder to produce the generated marker pattern I_t^G . During inference, we utilize the mean of the VAE posterior distribution instead of random sampling to ensure deterministic outputs.

Training for marker encoder-decoder. The marker encoder was trained on simulated arbitrary marker deformation dataset collected across 12 various marker patterns. The dataset was organized in a location-paired structure, where each source pattern was matched with corresponding target patterns captured under the same contact location. We employed an 80-20 train-test split with a fixed random seed for reproducibility. All images were preprocessed to a uniform size of 256×256 pixels and normalized to $[0,1]$ range. The training utilized permutations of pattern pairs, where for each surface type, every pattern type served as both source and target, creating a comprehensive set of translation scenarios in total of $12 \times 11 = 132$ source-target combinations. Each training sample in one batch consisted of a triplet: a source marker image I_t^S , its corresponding target marker image I_t^T , and a reference pattern image I_0^T representing the desired target pattern type. The model was trained using AdamW optimizer with a learning rate of 1e-4, betas=(0.9, 0.999), and weight decay of 1e-2. We employed mixed-precision training (FP16) with a batch size of 16. The loss function combined reconstruction loss (L1 + L2) and KL divergence with weights of 1.0 and 1e-6 respectively. Training proceeded for 100,000 steps.

Training for M2M model. The training process consisted of two main stages: pre-training on simulated data followed by fine-tuning on real-world datasets. Initially, the

image-conditioned diffusion model was trained on the simulated paired tactile sensor dataset. After achieving convergence on the simulated dataset, the model was fine-tuned on three distinct real-world tactile sensor datasets, each addressing different aspects of tactile sensing. The first dataset focused on homogeneous sensor translations across five sensors, with certain surface types (e.g., sphere, triangle, pacman, cone, wave, torus) held out as an unseen test set to evaluate generalization capability. The second dataset addressed the material compensation problem by incorporating seven variants of GelSight sensors with skins of varying softness. The third dataset tackled heterogeneous sensor translations between three fundamentally different tactile sensor types (GelSight, uSkin, and TacTip).

The model was optimized using a multi-component loss function:

$$\mathcal{L} = \lambda_{\text{gan}} \mathcal{L}_{\text{gan}} + \lambda_{\text{lpipl}} \mathcal{L}_{\text{lpipl}} + \lambda_{\text{l2}} \mathcal{L}_{\text{l2}} \quad (5)$$

where $\lambda_{\text{gan}} = 0.5$, $\lambda_{\text{lpipl}} = 5.0$, and $\lambda_{\text{l2}} = 1.0$ balance the contributions of adversarial, perceptual, and reconstruction losses respectively. We employed a CLIP-based vision-aided discriminator with multilevel sigmoid loss for the adversarial component, and a VGG-based LPIPS network for perceptual loss computation. The model was trained using AdamW optimizer with an initial learning rate of 5e-6, betas=(0.9, 0.999), epsilon=1e-8, and weight decay of 1e-2. Training proceeded with a batch size of 16 for a maximum of 100,000 steps, with gradient accumulation steps of 1 and gradient clipping at 1.0. The learning rate was managed using a scheduler with 500 warmup steps.

Inference Process. For model inference, we developed three specialized dataset handlers to accommodate different testing scenarios: simulated marker patterns (SimDataset), real-world homogeneous sensors (InferDatasetReal), and heterogeneous sensor translations (InferDatasetHetero). Each dataset was preprocessed using consistent image transformations, including resizing to 256×256 pixels and normalization. For real-world data, binary images were handled in both compressed (.npy) and standard image (.jpg) formats, with appropriate thresholding (>50 for .jpg, unpackbits for compressed .npy) to ensure consistent marker representation. During inference, the model processed images in batches of 8, generating predictions that were subsequently upscaled to the target resolution (640×480) using Lanczos interpolation. The upscaled outputs underwent adaptive thresholding to produce binary marker patterns, with an optional quality check counting the number of detected markers (threshold set to 80 markers for certain sensor types). The results were saved either as compressed binary

numpy arrays or as JPEG images, maintaining the original directory structure to facilitate direct comparisons. For systematic evaluation, we generated translations between all possible sensor pairs ($N \times (N - 1)$ combinations for N sensors), with additional flexibility to target specific sensor types as the output domain.

Spatio-temporal force prediction model

Model architecture. We designed a deep learning architecture that combines spatial feature extraction with temporal modeling to predict contact forces from tactile image sequences. The model consists of four main components: a marker feature encoder backbone from RAFT [71], a spatio-temporal module (convolutional GRU, ConvGRU), a post-processing network with ResNet Unit, and a regression head with multilayer perceptron (MLP). The input to our model is a sequence of tactile images with shape $S \times B \times 3 \times 256 \times 256$, where S is the sequence length, B is the batch size, and each image has 3 channels with 256×256 spatial resolution. The marker feature encoder processes these images through three convolutional blocks, each incorporating instance normalization and dropout. The first block reduces spatial dimensions to 128×128 while increasing channels to 64, the second block further reduces to 64×64 with 96 channels, and the third block outputs features at 32×32 resolution with 128 channels. These spatial features are then processed by a ConvGRU module that maintains the 32×32 spatial resolution while capturing temporal dependencies across the sequence. With a hidden state dimension of 128 channels, the ConvGRU tracks temporal patterns while preserving spatial information. The temporal features undergo spatial dimension reduction through two residual blocks (stride 2), expanding the channel dimension from 128 to 256, then to 512, while reducing spatial dimensions to 16×16 and 8×8 respectively. An adaptive average pooling layer collapses the remaining spatial dimensions to 1×1 , producing a 512-dimensional feature vector per timestep. The regression head maps these features to 3D force predictions using a fully connected layer followed by sigmoid activation. This architecture effectively combines spatial and temporal processing to capture both the detailed surface deformations in individual frames and their evolution over time, enabling accurate prediction of 3D contact forces from tactile image sequences.

Model Training. The training process begins with data preparation through our custom sequential dataset loader, which handles both tactile images and corresponding force measurements. The image data undergoes preprocessing including resizing to 256×256 pixels and normalization using ImageNet statistics (mean=[0.485, 0.456,

$0.406]$, $\text{std}=[0.229, 0.224, 0.225]$). Force measurements are normalized using pre-computed global minimum and maximum values to ensure consistent scaling across different samples. Our dataloader implements dynamic sequence sampling, where for each batch, we randomly sample sequence lengths between first frame and the maximum available length with at least two frames, enabling the model to learn from varying temporal contexts. For model initialization, we employ Kaiming normalization for convolutional layers and constant initialization for normalization layers. The training process follows a two-stage approach: first, we pre-train the model on a single randomly selected sensor with a learning rate of 1×10^{-1} for 40 epochs, then fine-tune on the complete dataset with a learning rate of 1×10^{-3} for another 40 epochs. We use SGD optimization with momentum (0.9) and weight decay (5×10^{-4}), along with a learning rate scheduler for flexible parameter updates. During training, we utilize a custom collate function that handles varying sequence lengths through dynamic padding, where shorter sequences are padded to match the batch's sampled sequence length by repeating the last frame. The model is trained with a batch size of 4 using L1 loss between predicted and ground truth forces, exclusively on the seen group data, with early stopping based on validation performance.

Model Inference. During inference, our model processes tactile image sequences to predict 3D contact forces. The inference pipeline utilizes a modified data loading scheme where, unlike training, we process the complete sequence length without random sampling. The dataloader maintains the same image preprocessing pipeline (resizing to 256×256 and normalization with ImageNet statistics) but handles sequences deterministically. For both source and target domain evaluation, we load full sequences with a batch size of 1 to ensure consistent temporal processing across all samples. The predictions undergo denormalization using globally tracked minimum and maximum force values same as training to restore the actual force scale. We evaluate the model's performance using multiple metrics: Mean Absolute Error (MAE) for individual force components (F_x, F_y, F_z), MAE for total force magnitude, and R^2 scores to assess prediction accuracy. The evaluation is conducted on all dataset or separately on seen (source) and unseen (target) sensor data to assess generalization capability. For each prediction, we compute per-axis errors and total force errors using L1 loss, maintaining running averages for comprehensive performance assessment. This evaluation framework provides a thorough assessment of the model's ability to capture both component-wise force predictions and overall force magnitudes across different tactile sensors.

Material Compensation

Tactile sensors often operate in diverse environments, necessitating customization of the Young’s modulus in their outermost elastomer layer. However, variations in Young’s modulus between source and target domain sensors can significantly impact our force prediction model’s performance when using location-paired datasets. Target domain sensors may incorporate elastomers that are either softer or harder than their source domain counterparts. Consequently, directly transferring force labels from source to target domains for paired images collected at identical contact depths can lead to systematic under- or over-estimation, depending on the relative elastomer hardness. To address this challenge, we propose a material compensation method that adjusts pseudo force labels by leveraging prior knowledge of Young’s modulus differences between source and target sensors. This compensation mechanism accounts for variations in elastomer properties, ensuring consistent performance across diverse sensor configurations.

Relationship of Force and Indentation Depth. According to contact mechanics, when a flat rigid indenter applies force F on an elastic specimen’s surface [72], the relationship between force F and penetration depth d_z is given by:

$$F = \alpha E^* d_z \quad (6)$$

where α is a geometric constant specific to the indenter, and E^* represents the combined elastic modulus of the indenter (E') and specimen (E). In our case, $E^* = E$ as the pressure distribution remains uniform under the flat surface of the rigid indenter.

Material Prior Data Collection. Based on Equation 6, we characterized the modulus relationship between applied force F and indentation depth d_z using seven elastomer variants with different softness levels, achieved by adjusting the XPA-565 ratio for GelSight as described in Section 4. For homogeneous sensor testing, we conducted three repetitions of indentation tests using a prism indenter with a flat rigid surface, pressing to a maximum depth of 1.2mm while collecting paired force-depth data during both loading and unloading phases. This dual-phase collection accounts for the material’s inherent hysteresis, where identical depths yield different forces during loading versus unloading. For heterogeneous testing, we applied maximum depths of 1mm for GelSight and uSkin, while extending to 4.5mm for TacTip due to its significantly softer composition. For heterogeneous sensors, we normalized all indentation depths to a 0-1 range to facilitate cross-sensor comparison.

References

- [1] Lee, M.H.: Tactile sensing: new directions, new challenges. *The International journal of robotics research* **19**(7), 636–643 (2000)
- [2] Silvera-Tawil, D., Rye, D., Velonaki, M.: Artificial skin and tactile sensing for socially interactive robots: A review. *Robotics and Autonomous Systems* **63**, 230–243 (2015)
- [3] Chen, T., Tippur, M., Wu, S., Kumar, V., Adelson, E., Agrawal, P.: Visual dexterity: In-hand reorientation of novel and complex object shapes. *Science Robotics* **8**(84), 9244 (2023)
- [4] Yang, M., Lu, C., Church, A., Lin, Y., Ford, C., Li, H., Psomopoulou, E., Barton, D.A., Lepora, N.F.: Anyrotate: Gravity-invariant in-hand object rotation with sim-to-real touch. *arXiv preprint arXiv:2405.07391* (2024)
- [5] Gardner, E.P.: *Touch*. eLS (2010)
- [6] Goodwin, A.W.: *Somatosensory systems*. eLS (2005)
- [7] Dahiya, R.S., Metta, G., Valle, M., Sandini, G.: Tactile sensing—from humans to humanoids. *IEEE Transactions on Robotics* **26**(1), 1–20 (2010)
- [8] Lee, S., Franklin, S., Hassani, F.A., Yokota, T., Nayeem, M.O.G., Wang, Y., Leib, R., Cheng, G., Franklin, D.W., Someya, T.: Nanomesh pressure sensor for monitoring finger manipulation without sensory interference. *Science* **370**(6519), 966–970 (2020)
- [9] Shih, B., Shah, D., Li, J., Thuruthel, T.G., Park, Y.-L., Iida, F., Bao, Z., Kramer-Bottiglio, R., Tolley, M.T.: Electronic skins and machine learning for intelligent soft robots. *Science Robotics* **5**(41), 9239 (2020)
- [10] Wang, S., She, Y., Romero, B., Adelson, E.: GelSight wedge: Measuring high-resolution 3d contact geometry with a compact robot finger. In: *ICRA*, pp. 6468–6475 (2021)
- [11] Ward-Cherrier, B., Pestell, N., F, N., *et al.*: The TacTip family: Soft optical tactile sensors with 3d-printed biomimetic morphologies. *Soft robotics* **5**(2), 216–227 (2018)

- [12] Zhao, J., Adelson, E.H.: GelSight Svelte: A human finger-shaped single-camera tactile robot finger with large sensing coverage and proprioceptive sensing. In: IROS, pp. 8979–8984 (2023)
- [13] Huang, Y., Zhou, J., Ke, P., Guo, X., Yiu, C.K., Yao, K., Cai, S., Li, D., Zhou, Y., Li, J., *et al.*: A skin-integrated multimodal haptic interface for immersive tactile feedback. *Nature Electronics* **6**(12), 1020–1031 (2023)
- [14] Sun, Z., Zhang, Z., Lee, C.: A skin-like multimodal haptic interface. *Nature Electronics* **6**(12), 941–942 (2023)
- [15] Tee, B.C.-K., Chortos, A., Berndt, A., Nguyen, A.K., Tom, A., McGuire, A., Lin, Z.C., Tien, K., Bae, W.-G., Wang, H.l., *et al.*: A skin-inspired organic digital mechanoreceptor. *Science* **350**(6258), 313–316 (2015)
- [16] Zhu, H., Luo, H., Cai, M., Song, J.: A multifunctional flexible tactile sensor based on resistive effect for simultaneous sensing of pressure and temperature. *Advanced Science* **11**(6), 2307693 (2024)
- [17] Liu, Z., Hu, X., Bo, R., Yang, Y., Cheng, X., Pang, W., Liu, Q., Wang, Y., Wang, S., Xu, S., *et al.*: A three-dimensionally architected electronic skin mimicking human mechanosensation. *Science* **384**(6699), 987–994 (2024)
- [18] Chen, Z., Zhang, Y., Zhu, B., Wu, Y., Du, X., Lin, L., Wu, D.: Laser-sculptured hierarchical spinous structures for ultra-high-sensitivity iontronic sensors with a broad operation range. *ACS Applied Materials & Interfaces* **14**(17), 19672–19682 (2022)
- [19] Zhang, J., Yao, H., Mo, J., Chen, S., Xie, Y., Ma, S., Chen, R., Luo, T., Ling, W., Qin, L., *et al.*: Finger-inspired rigid-soft hybrid tactile sensor with superior sensitivity at high frequency. *Nature communications* **13**(1), 5076 (2022)
- [20] Yan, Y., Hu, Z., Yang, Z., Yuan, W., Song, C., Pan, J., Shen, Y.: Soft magnetic skin for super-resolution tactile sensing with force self-decoupling. *Science Robotics* **6**(51), 8801 (2021)
- [21] Zatsiorsky, V.M., Latash, M.L.: Multifinger prehension: an overview. *Journal of motor behavior* **40**(5), 446–476 (2008)
- [22] Li, S.: Perception of individual finger forces during multi-finger force production

tasks. *Neuroscience letters* **409**(3), 239–243 (2006)

[23] Latash, M.L., Danion, F., Scholz, J.F., Zatsiorsky, V.M., Schöner, G.: Approaches to analysis of handwriting as a task of coordinating a redundant motor system. *Human movement science* **22**(2), 153–171 (2003)

[24] Deng, Z., Jonetzko, Y., Zhang, L., Zhang, J.: Grasping force control of multi-fingered robotic hands through tactile sensing for object stabilization. *Sensors* **20**(4), 1050 (2020)

[25] Romano, J.M., Hsiao, K., Niemeyer, G., Chitta, S., Kuchenbecker, K.J.: Human-inspired robotic grasp control with tactile sensing. *IEEE Transactions on Robotics* **27**(6), 1067–1079 (2011)

[26] Hang, K., Li, M., Stork, J.A., Bekiroglu, Y., Pokorny, F.T., Billard, A., Kragic, D.: Hierarchical fingertip space: A unified framework for grasp planning and in-hand grasp adaptation. *IEEE Transactions on robotics* **32**(4), 960–972 (2016)

[27] Johansson, R.S., Flanagan, J.R.: Coding and use of tactile signals from the fingertips in object manipulation tasks. *Nature Reviews Neuroscience* **10**(5), 345–359 (2009)

[28] Zhang, L., Wang, Y., Jiang, Y.: Tac3d: A novel vision-based tactile sensor for measuring forces distribution and estimating friction coefficient distribution. *arXiv preprint arXiv:2202.06211* (2022)

[29] Li, H., Nam, S., Lu, Z., Yang, C., Psomopoulou, E., Lepora, N.F.: Biotactip: A soft biomimetic optical tactile sensor for efficient 3d contact localization and 3d force estimation. *RA-L* (2024)

[30] Ma, D., Donlon, E., Dong, S., Rodriguez, A.: Dense tactile force estimation using gelslim and inverse fem. In: *ICRA*, pp. 5418–5424 (2019)

[31] Taylor, I.H., Dong, S., Rodriguez, A.: Gelslim 3.0: High-resolution measurement of shape, force and slip in a compact tactile-sensing finger. In: *ICRA*, pp. 10781–10787 (2022)

[32] Fernandez, A.J., Weng, H., Umphanhowar, P.B., Lynch, K.M.: Visiflex: A low-cost compliant tactile fingertip for force, torque, and contact sensing. *IEEE Robotics and Automation Letters* **6**(2), 3009–3016 (2021)

- [33] Melly, S.K., Liu, L., Liu, Y., Leng, J.: A review on material models for isotropic hyperelasticity. *International Journal of Mechanical System Dynamics* **1**(1), 71–88 (2021)
- [34] Sun, H., Kuchenbecker, K.J., Martius, G.: A soft thumb-sized vision-based sensor with accurate all-round force perception. *Nature Machine Intelligence* **4**(2), 135–145 (2022)
- [35] Do, W.K., Jurewicz, B., Kennedy, M.: Densetact 2.0: Optical tactile sensor for shape and force reconstruction. In: ICRA, pp. 12549–12555 (2023)
- [36] Lin, C., Zhang, H., Xu, J., Wu, L., Xu, H.: 9dtact: A compact vision-based tactile sensor for accurate 3d shape reconstruction and generalizable 6d force estimation. *RA-L* (2023)
- [37] Zhuang, F., Qi, Z., Duan, K., Xi, D., Zhu, Y., Zhu, H., Xiong, H., He, Q.: A comprehensive survey on transfer learning. *Proceedings of the IEEE* **109**(1), 43–76 (2021)
- [38] Feng, R., Hu, J., Xia, W., Gao, T., Shen, A., Sun, Y., Fang, B., Hu, D.: Anytouch: Learning unified static-dynamic representation across multiple visuo-tactile sensors. *arXiv preprint arXiv:2502.12191* (2025)
- [39] Gupta, H., Mo, Y., Jin, S., Yuan, W.: Sensor-invariant tactile representation. In: The Thirteenth International Conference on Learning Representations (2025)
- [40] Zhao, J., Ma, Y., Wang, L., Adelson, E.H.: Transferable tactile transformers for representation learning across diverse sensors and tasks. *arXiv preprint arXiv:2406.13640* (2024)
- [41] Sferrazza, C., D’Andrea, R.: Transfer learning for vision-based tactile sensing. In: IROS, pp. 7961–7967 (2019). <https://doi.org/10.1109/IROS40897.2019.8967571>
- [42] Yang, F., Feng, C., Chen, Z., Park, H., Wang, D., Dou, Y., Zeng, Z., Chen, X., Gangopadhyay, R., Owens, A., *et al.*: Binding touch to everything: Learning unified multimodal tactile representations. In: Proceedings of the IEEE/CVF Conference on Computer Vision and Pattern Recognition, pp. 26340–26353 (2024)

- [43] Higuera, C., Sharma, A., Bodduluri, C.K., Fan, T., Lancaster, P., Kalakrishnan, M., Kaess, M., Boots, B., Lambeta, M., Wu, T., et al.: Sparsh: Self-supervised touch representations for vision-based tactile sensing. arXiv preprint arXiv:2410.24090 (2024)
- [44] Rodriguez, S., Dou, Y., Oller, M., Owens, A., Fazeli, N.: Touch2touch: Cross-modal tactile generation for object manipulation. arXiv preprint arXiv:2409.08269 (2024)
- [45] Amri, W.Z.E., Kuhlmann, M., Navarro-Guerrero, N.: Across: A deformation-based cross-modal representation for robotic tactile perception. arXiv preprint arXiv:2411.08533 (2024)
- [46] Grella, F., Albini, A., Cannata, G., Maiolino, P.: Touch-to-touch translation—learning the mapping between heterogeneous tactile sensing technologies. arXiv preprint arXiv:2411.02187 (2024)
- [47] Harris, J.A., Harris, I.M., Diamond, M.E.: The topography of tactile working memory. *Journal of Neuroscience* **21**(20), 8262–8269 (2001)
- [48] Harris, J.A., Miniussi, C., Harris, I.M., Diamond, M.E.: Transient storage of a tactile memory trace in primary somatosensory cortex. *Journal of Neuroscience* **22**(19), 8720–8725 (2002)
- [49] Gallace, A., Spence, C.: The cognitive and neural correlates of tactile memory. *Psychological bulletin* **135**(3), 380 (2009)
- [50] Goodfellow, I., Pouget-Abadie, J., Mirza, M., Xu, B., Warde-Farley, D., Ozair, S., Courville, A., Bengio, Y.: Generative adversarial nets. *NeurIPS* **27** (2014)
- [51] Luu, Q.K., Nguyen, N.H., et al.: Simulation, learning, and application of vision-based tactile sensing at large scale. *IEEE Transactions on Robotics* **39**(3), 2003–2019 (2023)
- [52] Fan, W., Li, H., Si, W., Luo, S., Lepora, N., Zhang, D.: Vitactip: Design and verification of a novel biomimetic physical vision-tactile fusion sensor. arXiv preprint arXiv:2402.00199 (2024)
- [53] Kim, W.D., Yang, S., Kim, W., Kim, J.-J., Kim, C.-H., Kim, J.: Marker-embedded

tactile image generation via generative adversarial networks. *RA-L* **8**(8), 4481–4488 (2023)

[54] Rao, K., Harris, C., Irpan, A., Levine, S., Ibarz, J., Khansari, M.: Rl-cyclegan: Reinforcement learning aware simulation-to-real. In: *CVPR*, pp. 11157–11166 (2020)

[55] Rombach, R., Blattmann, A., Lorenz, D., Esser, P., Ommer, B.: High-resolution image synthesis with latent diffusion models. In: *Proceedings of the IEEE/CVF Conference on Computer Vision and Pattern Recognition*, pp. 10684–10695 (2022)

[56] Saharia, C., Chan, W., Chang, H., Lee, C., Ho, J., Salimans, T., Fleet, D., Norouzi, M.: Palette: Image-to-image diffusion models. In: *ACM SIGGRAPH 2022 Conference Proceedings*, pp. 1–10 (2022)

[57] Zhong, S., Albini, A., Maiolino, P., Posner, I.: Tactgen: Tactile sensory data generation via zero-shot sim-to-real transfer. *IEEE Transactions on Robotics* (2024)

[58] Lin, X., Xu, W., Mao, Y., Wang, J., Lv, M., Liu, L., Luo, X., Li, X.: Vision-based tactile image generation via contact condition-guided diffusion model. *arXiv preprint arXiv:2412.01639* (2024)

[59] Chen, Z., Ou, N., Zhang, X., Luo, S.: Transforce: Transferable force prediction for vision-based tactile sensors with sequential image translation. *arXiv preprint arXiv:2409.09870* (2024)

[60] Chen, Z., Ou, N., Jiang, J., Luo, S.: Deep domain adaptation regression for force calibration of optical tactile sensors. In: *2024 IEEE/RSJ International Conference on Intelligent Robots and Systems (IROS)*, pp. 13561–13568 (2024). IEEE

[61] Shahidzadeh, A.-H., Caddeo, G., Alapati, K., Natale, L., Fermüller, C., Aloimonos, Y.: Feelanyforce: Estimating contact force feedback from tactile sensation for vision-based tactile sensors. *arXiv preprint arXiv:2410.02048* (2024)

[62] Chen, Z., Zhang, S., Luo, S., Sun, F., Fang, B.: Tacchi: A pluggable and low computational cost elastomer deformation simulator for optical tactile sensors. *IEEE Robotics and Automation Letters* **8**(3), 1239–1246 (2023)

- [63] Romero, B., Fang, H.-S., Agrawal, P., Adelson, E.: Eyesight hand: Design of a fully-actuated dexterous robot hand with integrated vision-based tactile sensors and compliant actuation. In: 2024 IEEE/RSJ International Conference on Intelligent Robots and Systems (IROS), pp. 1853–1860 (2024). IEEE
- [64] Wang, M., Li, W., Liang, H., Li, B., Althoefer, K., Su, Y., Liu, H.: Large-scale deployment of vision-based tactile sensors on multi-fingered grippers. In: 2024 IEEE/RSJ International Conference on Intelligent Robots and Systems (IROS), pp. 13946–13952 (2024). IEEE
- [65] Bauza, M., Chen, J.E., Dalibard, V., Gileadi, N., Hafner, R., Martins, M.F., Moore, J., Pevcovicu, R., Laurens, A., Rao, D., et al.: Demostart: Demonstration-led auto-curriculum applied to sim-to-real with multi-fingered robots. arXiv preprint arXiv:2409.06613 (2024)
- [66] Yuan, W., Dong, S., Adelson, E.H.: GelSight: High-resolution robot tactile sensors for estimating geometry and force. Sensors **17**(12), 2762 (2017)
- [67] Zhang, X., Yang, T., Zhang, D., Lepora, N.F.: Tacpalm: A soft gripper with a biomimetic optical tactile palm for stable precise grasping. IEEE Sensors Journal (2024)
- [68] Xiong, Y., Varadarajan, B., Wu, L., Xiang, X., Xiao, F., Zhu, C., Dai, X., Wang, D., Sun, F., Iandola, F., et al.: Efficientsam: Leveraged masked image pretraining for efficient segment anything. In: Proceedings of the IEEE/CVF Conference on Computer Vision and Pattern Recognition, pp. 16111–16121 (2024)
- [69] Parmar, G., Park, T., Narasimhan, S., Zhu, J.-Y.: One-step image translation with text-to-image models. arXiv preprint arXiv:2403.12036 (2024)
- [70] Sauer, A., Lorenz, D., Blattmann, A., Rombach, R.: Adversarial diffusion distillation. In: European Conference on Computer Vision, pp. 87–103 (2024). Springer
- [71] Teed, Z., Deng, J.: Raft: Recurrent all-pairs field transforms for optical flow. In: ECCV, pp. 402–419 (2020)
- [72] Fischer-Cripps, A.C.: Introduction to Contact Mechanics vol. 101, pp. 126–127 (2007)